Numerical study of time-splitting spectral discretizations of nonlinear Schrödinger equations in the semi-classical regimes

Weizhu Bao *
Department of Computational Science
National University of Singapore, Singapore 117543

Shi Jin †
Department of Mathematics, University of Wisconsin-Madison
Madison, WI 53706, USA

Peter A. Markowich ‡
Institute of Mathematics, University of Vienna
Boltzmanngasse 9, A-1090 Vienna, Austria

Abstract

In this paper we study the performance of time-splitting spectral approximations for general nonlinear Schrödinger equations (NLS) in the semiclassical regimes, where the Planck constant ε is small. The spectral time-splitting approximation under study is explicit, unconditionally stable and conserves the position density in L^1. Moreover it is time-transverse invariant and time reversible when the corresponding nonlinear Schrödinger equation is. Extensive numerical tests are presented for weak/strong focusing/defocusing nonlinearities, for the Gross-Pitaevskii equation and for current-relaxed quantum hydrodynamics. The tests are geared towards the understanding of admissible meshing strategies for obtaining 'correct' physical observables in the semi-classical regimes. Furthermore, comparisons between the solutions of the nonlinear Schrödinger equation and its hydrodynamic semiclassical limit are presented.

*Email address: bao@cz3.nus.edu.sg.
†Email address: jin@math.wisc.edu.
‡Email address: peter.markowich@univie.ac.at.

Key Words: Nonlinear Schrödinger equation (NLS), spectral time-splitting approximation, semiclassical regime, meshing strategy, Gross-Pitaevskii equation, physical observable.

1 Introduction

Many problems of solid state physics require the solution of the following general nonlinear Schrödinger equation (NLS) with a small (scaled) Planck constant ε ($0 < \varepsilon \ll 1$):

$$i\varepsilon u_t^\varepsilon + \frac{\varepsilon^2}{2}\,\Delta u^\varepsilon - V\,u^\varepsilon - f(|u^\varepsilon|^2)u^\varepsilon - \varepsilon\tau\,\arg(u^\varepsilon)u^\varepsilon = 0,\ t > 0,\ \mathbf{x} \in \mathbb{R}^d, \quad (1.1)$$

$$u^\varepsilon(\mathbf{x}, t = 0) = u_0^\varepsilon(\mathbf{x}), \qquad \mathbf{x} \in \mathbb{R}^d. \quad (1.2)$$

In this equation, $V = V(\mathbf{x})$ is a given real-valued electrostatic potential, f is a real-valued smooth function, $\tau \geq 0$ is a constant relaxation rate, $u^\varepsilon = u^\varepsilon(\mathbf{x}, t)$ is the (complex-valued) wave function and $\arg(u^\varepsilon)$ is defined (up to an additive constant) as:

$$\varepsilon \arg(u^\varepsilon(\mathbf{x}, t)) = S^\varepsilon(\mathbf{x}, t), \qquad \nabla S^\varepsilon = J^\varepsilon/\rho^\varepsilon, \quad \text{when } \rho^\varepsilon \neq 0, \quad (1.3)$$

where ρ^ε (the position density) and J^ε (the current density) are primary physical quantities and can be computed from the wave function u^ε:

$$\rho^\varepsilon(\mathbf{x}, t) = |u^\varepsilon(\mathbf{x}, t)|^2, \quad (1.4)$$

$$J^\varepsilon(\mathbf{x}, t) = \varepsilon\ \mathrm{Im}(\overline{u^\varepsilon(\mathbf{x}, t)}\ \nabla u^\varepsilon(\mathbf{x}, t)). \quad (1.5)$$

Here "—" denotes complex conjugation.

The general form of (1.1) covers many (non)linear Schrödinger equations arising in various different applications. For example, when $f \equiv 0$ and $\tau = 0$, (1.1) reduces to the linear Schrödinger equation; when $V \equiv 0$, $f(\rho) = \beta_\varepsilon\,\rho$ and $\tau = 0$, it is the cubic nonlinear Schrödinger equation (called the focusing NLS if $\beta_\varepsilon < 0$ and the defocusing NLS if $\beta_\varepsilon > 0$); when $V(\mathbf{x}) = \frac{\omega}{2}|\mathbf{x}|^2$ with $\omega > 0$ a constant, $f(\rho) = \rho$ and $\tau = 0$, it is related to Bose-Einstein condensation (Gross-Pitaevskii equation, cf. [12]). For $\tau > 0$ the equation can be rewritten as current-relaxed quantum hydrodynamical system for ρ^ε and J^ε (cf. [22, 23, 26]). It is well known that the equation (1.1) propagates oscillations in space and time, preventing u^ε from converging strongly as $\varepsilon \to 0$. On the other hand, the weak convergence of u^ε is, for example, not sufficient for passing to the limit in the quadratic macroscopic densities (1.4)–(1.5). The analysis of the so-called semiclassical limit is a mathematically complex issue.

Much progress has been made recently in understanding semiclassical limits of the linear Schödinger equation, particularly by the introduction of tools from microlocal analysis, such as defect measures [14], H-measures [33], and Wigner measures [13, 15, 27]. These techniques have provided powerful technical tools to exploit properties of the linear Schrödinger equation in the semiclassical limit regime, allowing the passage to the limit $\varepsilon \to 0$ in the macroscopic densities by revealing an

underlying kinetic structure. However, they techniques have not been successfully extended to the semiclassical limit of the (cubically) nonlinear Schrödinger equation, which was solved in the one-dimensional defocusing nonlinearity using techniques of inverse scattering [19, 20]. For results regarding the semiclassical limit of the focusing nonlinear Schrödinger equation see [7, 30, 11, 9].

The oscillatory nature of the solutions of the Schrödinger equation with small ε provides severe numerical burdens. Even for stable numerical approximations (or under mesh size and time step restrictions which guarantee stability) the oscillations may very well pollute the solution in such a way that the quadratic macroscopic quantities and other physical observables come out completely wrong unless the spatial-temporal oscillations are fully resolved numerically, i.e., using many grid points per wave length of $O(\varepsilon)$. In [28, 29], Markowich at. el. studied the finite difference approximation of the linear Schrödinger equation with small ε. Their results show that, for the best combination of the time and space discretizations, one needs the following constraints in order to guarantee good approximations to all (smooth) observables for ε small [28, 29]:

$$\text{mesh size } h = o(\varepsilon), \qquad \text{time step } k = o(\varepsilon). \tag{1.6}$$

Failure to satisfy these conditions leads to wrong numerical observables. In [3], we studied the time-splitting spectral approximation for the linear Schrödinger equation. We proved the following meshing strategy which guarantees good approximations of all observables for ε small [3]:

$$h = O(\varepsilon), \qquad k \text{ independent of } \varepsilon. \tag{1.7}$$

In this paper we systematically study the time-splitting spectral discretizations of the general nonlinear Schrödinger equation in the semiclassical regimes (1.1), (1.2). Such a discretization was studied previously for $\varepsilon = O(1)$ in [32], which does not give any clue for its performance in the semiclassical regimes, where $\varepsilon << 1$. Since the semi-classical limit behavior of nonlinear Schrödinger equations is largely unknown, a scheme that performs well (allowing largest possible mesh size and time step for a given ε) is important for the investigations of the semi-classical behavior of NLS and to predict their semi-classical limits.

The goal of this paper is to understand the resolution capacity and mesh strategies of the time-splitting spectral method for NLS and investigate the semiclassical limit of the NLS numerically by using the time-splitting spectral method. Our numerical experiments suggest the following meshing strategies for obtaining the correct observables: $k = O(\varepsilon)$ and $h = O(\varepsilon)$ for defocusing nonlinearities and weak $O(\varepsilon)$ focusing nonlinearities; $k = o(\varepsilon)$ and $h = O(\varepsilon)$ for strong $O(1)$ focusing nonlinearities (when the Krasny Filter is applied). Furthermore, comparisons between the solutions of the nonlinear Schrödinger equation and its formal hydrodynamic semiclassical limit are presented.

The paper is organized as follows. In section 2 we present the formal semiclassical limit of the NLS (1.1). In section 3 we discuss time-splitting spectral discretizations

of the NLS (1.1), (1.2) in 1-d. In section 4 numerical tests for different types of NLS are presented. Further comparisons between the solutions of the nonlinear Schrödinger equation and its hydrodynamical semiclassical limit are also made. In section 5 some conclusions are drawn.

2 Formal semiclassical limit

Suppose that the initial datum u_0^ε in (1.2) is rapidly oscillating on the scale ε, given in WKB form:

$$u_0^\varepsilon(\mathbf{x}) = A_0(\mathbf{x}) \exp\left(\frac{i}{\varepsilon} S_0(\mathbf{x})\right), \qquad \mathbf{x} \in \mathbb{R}^d, \tag{2.1}$$

where the amplitude A_0 and the phase S_0 are smooth real-valued functions. Plugging the radial-representation of the wave-function

$$u^\varepsilon(\mathbf{x},t) = A^\varepsilon(\mathbf{x},t) \exp\left(\frac{i}{\varepsilon} S^\varepsilon(\mathbf{x},t)\right) = \sqrt{\rho^\varepsilon(\mathbf{x},t)} \exp\left(\frac{i}{\varepsilon} S^\varepsilon(\mathbf{x},t)\right) \tag{2.2}$$

into (1.1), one obtains the following quantum hydrodynamic form of the Schrödinger equation for $\rho^\varepsilon = |A^\varepsilon|^2$, $J^\varepsilon = \rho^\varepsilon \nabla S^\varepsilon$ [25]

$$\rho_t^\varepsilon + \operatorname{div} J^\varepsilon = 0, \tag{2.3}$$

$$J_t^\varepsilon + \operatorname{div}\left(\frac{J^\varepsilon \otimes J^\varepsilon}{\rho^\varepsilon}\right) + \nabla P(\rho^\varepsilon) + \rho^\varepsilon \nabla V + \tau J^\varepsilon = \frac{\varepsilon^2}{4} \operatorname{div}(\rho^\varepsilon \nabla^2 \log \rho^\varepsilon); \tag{2.4}$$

with initial data

$$\rho^\varepsilon(\mathbf{x},0) = \rho_0^\varepsilon(\mathbf{x}) = |A_0(\mathbf{x})|^2, \qquad J^\varepsilon(\mathbf{x},0) = \rho_0^\varepsilon(\mathbf{x}) \nabla S_0(\mathbf{x}) = |A_0(\mathbf{x})|^2 \nabla S_0(\mathbf{x}), \tag{2.5}$$

(see Grenier [17], Jüngel [22, 23], Lin and Li [26] for mathematical analyses of this system). Here the hydrodynamic pressure $P(\rho)$ is related to the nonlinear potential $f(\rho)$ by

$$P(\rho) = \rho f(\rho) - \int_0^\rho f(s)\, ds, \tag{2.6}$$

i.e. f' is the enthalpy. Letting $\varepsilon \to 0+$, one obtains formally the following Euler system

$$\rho_t + \operatorname{div} J = 0, \tag{2.7}$$

$$J_t + \operatorname{div}\left(\frac{J \otimes J}{\rho}\right) + \nabla P(\rho) + \rho \nabla V + \tau J = 0. \tag{2.8}$$

Note that $\frac{1}{\tau}$ is the actual relaxation time. In the case $f' > 0$ we expect (2.7), (2.8) to be the 'rigorous' semiclassical limit of (1.1) as long as caustics do not occur, i.e. in the pre-breaking regime. After caustics the dispersive behavior of the NLS takes over and (2.7), (2.8) is not correct any more. Note that the nonlinear Schrödinger equation (1.1) is time reversible iff $\tau = 0$, i.e. iff no current relaxation occurs.

3 Time-splitting spectral approximations

In this section we present time-splitting Fourier spectral approximations of the NLS (1.1), (1.2) for periodic problems. For simplicity of notation we shall introduce the method in one space dimension ($d = 1$). Generalizations to $d > 1$ are straightforward for tensor product grids and the results remain valid without modifications. For $d = 1$, the problem becomes

$$i\varepsilon u_t^\varepsilon + \frac{\varepsilon^2}{2} u_{xx}^\varepsilon - V(x)u^\varepsilon - f(|u^\varepsilon|^2)u^\varepsilon - \varepsilon\tau \arg(u^\varepsilon)u^\varepsilon = 0,\ a < x < b,\ t > 0, \tag{3.1}$$

$$u^\varepsilon(x, t = 0) = u_0^\varepsilon(x),\ a \le x \le b, \tag{3.2}$$

$$u^\varepsilon(a, t) = u^\varepsilon(b, t), u_x^\varepsilon(a, t) = u_x^\varepsilon(b, t),\ t > 0. \tag{3.3}$$

Clearly, the nonlinear Schrödinger equation is time-reversible iff $\tau = 0$, so we could equally pose (3.1) for $t \in \mathbb{R}$ in this case.

We choose the spatial mesh size $h = \Delta x > 0$ with $h = (b - a)/M$ for M an even positive integer, the time step $k = \Delta t > 0$ and let the grid points and the time step be

$$x_j := a + j\ h, \qquad t_n := n\ k, \qquad j = 0, 1, \cdots, M, \qquad n = 0, 1, 2, \cdots$$

Let $U_j^{\varepsilon,n}$ be the approximation of $u^\varepsilon(x_j, t_n)$ and $\mathbf{u}^{\varepsilon,n}$ be the solution vector at time $t = t_n = nk$ with components $U_j^{\varepsilon,n}$.

The first-order time-splitting spectral method (SP1). From time $t = t_n$ to $t = t_{n+1}$, the NLS equation (3.1) is solved in two steps. One solves first

$$i\varepsilon u_t^\varepsilon + \frac{\varepsilon^2}{2} u_{xx}^\varepsilon = 0, \tag{3.4}$$

for one time step (of length k), followed by solving

$$i\varepsilon u_t^\varepsilon - V(x)u^\varepsilon - f(|u^\varepsilon|^2)u^\varepsilon - \varepsilon\tau \arg(u^\varepsilon)u^\varepsilon = 0, \tag{3.5}$$

for the same time step. Equation (3.4) will be discretized in space by the Fourier spectral method and integrated in time *exactly*. For $t \in [t_n, t_{n+1}]$, the ODE (3.5) leaves $|u^\varepsilon|$ invariant in t:

$$\frac{\partial}{\partial t}\left(|u^\varepsilon|^2\right) = 2\ \mathrm{Re}(u_t^\varepsilon\ \overline{u^\varepsilon}) = -\frac{2}{\varepsilon}\ \mathrm{Re}\left(i\left(V(x) + f(|u^\varepsilon|^2) + \varepsilon\tau\ \arg(u^\varepsilon)\right)|u^\varepsilon|^2\right) = 0 \tag{3.6}$$

(since V and f are real valued) and therefore (3.5) becomes

$$i\varepsilon u_t^\varepsilon - V(x)u^\varepsilon - f(|u^\varepsilon(x, t_n)|^2)u^\varepsilon - \varepsilon\tau \arg(u^\varepsilon)u^\varepsilon = 0\,. \tag{3.7}$$

If $\tau = 0$, (3.7) can be integrated *exactly* and the solution is given by

$$u^\varepsilon(x, t) = e^{-i(V(x)+f(|u^\varepsilon(x,t_n)|^2))(t-t_n)/\varepsilon}\ u^\varepsilon(x, t_n), \qquad t \in [t_n, t_{n+1}]. \tag{3.8}$$

If $\tau \neq 0$, since $|u^\varepsilon|$ remains invariant for the ODE (3.7), we set

$$u^\varepsilon(x,t) = |u^\varepsilon(x,t_n)| \exp\left(\frac{i}{\varepsilon} S^\varepsilon(x,t)\right), \qquad t \in [t_n, t_{n+1}], \tag{3.9}$$

where S^ε is a function to be determined. Plugging (3.9) into (3.7), using (1.4) and (1.5), one obtains

$$S^\varepsilon_t(x,t) + \tau S^\varepsilon(x,t) + V(x) + f(|u^\varepsilon(x,t_n)|^2) = 0, \tag{3.10}$$

$$J^\varepsilon(x,t) = \rho^\varepsilon(x,t_n) S^\varepsilon_x(x,t). \tag{3.11}$$

Differentiating the equation (3.10) with respect to x gives

$$J^\varepsilon_t(x,t) + \tau J^\varepsilon(x,t) + \left[V_x(x) + f(|u^\varepsilon(x,t_n)|^2)_x\right] \rho(x,t_n) = 0\,. \tag{3.12}$$

Solving this ODE, one obtains

$$J^\varepsilon(x,t) = e^{-\tau(t-t_n)} J^\varepsilon(x,t_n) - \left[V_x(x) + f(|u^\varepsilon(x,t_n)|^2)_x\right] \rho(x,t_n) \frac{1-e^{-\tau(t-t_n)}}{\tau}. \tag{3.13}$$

For $\tau \neq 0$ we Substitute (3.13) into (3.11), and using (1.4) and (1.5), we find

$$\begin{aligned} S^\varepsilon_x(x,t) &= \frac{J^\varepsilon(x,t)}{\rho^\varepsilon(x,t_n)} \\ &= \frac{e^{-\tau(t-t_n)} J^\varepsilon(x,t_n)}{\rho^\varepsilon(x,t_n)} - \left[V_x(x) + f(|u^\varepsilon(x,t_n)|^2)_x\right] \frac{1-e^{-\tau(t-t_n)}}{\tau} \\ &= e^{-\tau(t-t_n)} \varepsilon \,\mathrm{Im}\left(\frac{u^\varepsilon_x(x,t_n)}{u^\varepsilon(x,t_n)}\right) - \left[V_x(x) + f(|u^\varepsilon(x,t_n)|^2)_x\right] \frac{1-e^{-\tau(t-t_n)}}{\tau} \end{aligned} \tag{3.14}$$

and set

$$\begin{aligned} \frac{S^\varepsilon(x,t)}{\varepsilon} &= e^{-\tau(t-t_n)} \int_a^x \mathrm{Im}\left(\frac{u^\varepsilon_v(v,t_n)}{u^\varepsilon(v,t_n)}\right) dv - \left[V(x) + f(|u^\varepsilon(x,t_n)|^2)\right] \frac{1-e^{-\tau(t-t_n)}}{\varepsilon\tau} \\ &= e^{-\tau(t-t_n)} \,\mathrm{Im}\left(\int_a^x \frac{u^\varepsilon_v(v,t_n)}{u^\varepsilon(v,t_n)}\, dv\right) - \left[V(x) + f(|u^\varepsilon(x,t_n)|^2)\right] \frac{1-e^{-\tau(t-t_n)}}{\varepsilon\tau} \\ &\equiv \mathcal{S}^\varepsilon(u^\varepsilon,t) - \left[V(x) + f(|u^\varepsilon(x,t_n)|^2)\right] \frac{1-e^{-\tau(t-t_n)}}{\varepsilon\tau}. \end{aligned} \tag{3.15}$$

Plugging (3.15) into (3.9), one obtains the solution of (3.5) in the case $\tau \neq 0$. Notice that $S^\varepsilon(x,t)$ is determined up to a constant and the choice of the constant does not affect the observables.

The detailed method is given by:

$$\begin{aligned} U_j^{\varepsilon,*} &= \frac{1}{M} \sum_{l=-M/2}^{M/2-1} e^{-i\varepsilon\mu_l^2 k/2}\, \widehat{U}_l^{\varepsilon,n}\, e^{i\mu_l(x_j-a)}, \qquad j = 0,1,2,\cdots,M-1, \\ U_j^{\varepsilon,n+1} &= \begin{cases} e^{-i(V(x_j)+f(|U_j^{\varepsilon,*}|^2))k/\varepsilon}\, U_j^{\varepsilon,*}, & \text{if } \tau = 0, \\ e^{-i(V(x_j)+f(|U_j^{\varepsilon,*}|^2))(1-e^{-k\tau})/\varepsilon\tau + i\mathcal{S}_j^\varepsilon(U^{\varepsilon,*},k)}\, |U_j^{\varepsilon,*}|, & \text{if } \tau \neq 0; \end{cases} \end{aligned} \tag{3.16}$$

where $\widehat{U}_l^{\varepsilon,n}$, the Fourier coefficients of $U^{\varepsilon,n}$, are defined as

$$\mu_l = \frac{2\pi l}{b-a}, \quad \widehat{U}_l^{\varepsilon,n} = \sum_{j=0}^{M-1} U_j^{\varepsilon,n}\, e^{-i\mu_l(x_j-a)},\ l = -\frac{M}{2}, \cdots, \frac{M}{2}-1, \tag{3.17}$$

with

$$U_j^{\varepsilon,0} = u^\varepsilon(x_j,0) = u_0^\varepsilon(x_j), \qquad j = 0,1,2,\cdots,M \tag{3.18}$$

and $\mathcal{S}^\varepsilon(U,k)$ is an approximation $\mathcal{S}^\varepsilon(u^\varepsilon,t)$ in (3.15). Here we use the composite trapezoidal rule to obtain $\mathcal{S}^\varepsilon$ numerically:

$$\mathcal{S}_j^\varepsilon(U,t) = e^{-\tau t}\sum_{l=1}^{j}\frac{h}{2}\,\mathrm{Im}\left(\frac{D_x^s\,U|_{x=x_{l-1}}}{U_{l-1}} + \frac{D_x^s\,U|_{x=x_l}}{U_l}\right), \tag{3.19}$$

$$j = 1,2,\cdots,M, \qquad S_0(U,k) = 0.$$

with D_x^s the spectral approximation of ∂_x:

$$D_x^s U|_{x=x_j} = \frac{1}{M}\sum_{l=-M/2}^{M/2-1} i\mu_l\ \widehat{U}_l\ e^{i\mu_l(x_j-a)}, \tag{3.20}$$

with

$$\widehat{U}_l = \sum_{j=0}^{M-1} U_j\ e^{-i\mu_l(x_j-a)},\ l = -\frac{M}{2}, \cdots, \frac{M}{2}-1. \tag{3.21}$$

Note that the only time discretization error of this method is the splitting error, which is $O(k)$ for any fixed $\varepsilon > 0$.

Remark 3.1 *If $\tau \neq 0$, the spectral accuracy in space is lost due to the use of the quadrature formula in (3.19). The spatial accuracy can easily be improved choosing high-order numerical integration for approximating the integral (3.15), using the spectral interpolant of $\mathbf{u}^{\varepsilon,n}$ for pointwise values of the integrand.*

The Strang splitting spectral method (SP2). From time $t = t_n$ to $t = t_{n+1}$, we combine the splitting steps via the standard Strang splitting:

$$\begin{aligned}
U_j^{\varepsilon,*} &= \begin{cases} e^{-i(V(x_j)+f(|U_j^{\varepsilon,n}|^2))k/2\varepsilon}\ U_j^{\varepsilon,n}, & \text{if } \tau = 0, \\ e^{-i(V(x_j)+f(|U_j^{\varepsilon,n}|^2))(1-e^{-k\tau})/2\varepsilon\tau + i\mathcal{S}_j^\varepsilon(U^{\varepsilon,n},k/2)}\ |U_j^{\varepsilon,n}|, & \text{if } \tau \neq 0, \end{cases} \\
U_j^{\varepsilon,**} &= \frac{1}{M}\sum_{l=-M/2}^{M/2-1} e^{-i\varepsilon\mu_l^2\,k/2}\ \widehat{U}_l^{\varepsilon,*}\ e^{i\mu_l(x_j-a)}, \qquad j = 0,1,2,\cdots,M-1, \\
U_j^{\varepsilon,n+1} &= \begin{cases} e^{-i(V(x_j)+f(|U_j^{\varepsilon,**}|^2))k/2\varepsilon}\ U_j^{\varepsilon,**}, & \text{if } \tau = 0, \\ e^{-i(V(x_j)+f(|U_j^{\varepsilon,**}|^2))(1-e^{-k\tau})/2\varepsilon\tau + i\mathcal{S}_j^\varepsilon(U^{\varepsilon,**},k/2)}\ |U_j^{\varepsilon,**}|, & \text{if } \tau \neq 0, \end{cases}
\end{aligned} \tag{3.22}$$

where $\widehat{U}_l^{\varepsilon,*}$, the Fourier coefficients of $U^{\varepsilon,*}$, are given by

$$\widehat{U}_l^{\varepsilon,*} = \sum_{j=0}^{M-1} U_j^{\varepsilon,*}\, e^{-i\mu_l(x_j-a)}, \qquad l = -\frac{M}{2}, \cdots, \frac{M}{2}-1\,, \tag{3.23}$$

and $S^\varepsilon(U,t)$ is as (3.19). The overall time discretization error now is $O(k^2)$ for fixed $\varepsilon > 0$.

Our numerical experiments later show that, when ε is small, SP1 and SP2 work very well for all considered cases except the strong O(1) focusing nonlinearity, i.e. $f(\rho) = -\beta\rho$ and $\beta = O(1) > 0$. In this case, due to the modulational instability (see [7]), the numerical solution is stable but qualitatively wrong for small ε with the accumulation of round-off errors. Therefore, we apply the Krasny filter [24] to the solution at each time step (see also [9] for similar applications). That is, we set to zero all the Fourier coefficients of the numerical solution whose magnitudes are below a certain filter threshold. In our numerical experiments, we take the threshold to be 10^{-12} as all our computations are performed with double precision arithmetic (with 15 accurate digits). This filter is applied only for the strong $O(1)$ focusing nonlinearity. It is not needed in all other cases.

For benchmark comparisons, we also define another spectral method, the *Crank-Nicolson type spectral method (CNSP)* which was proposed in [9] for the cubic focusing NLS ($V(x) \equiv 0$, $\tau = 0$ and $f(\rho) = -\rho$ in (3.1)):

$$\begin{aligned}
&\frac{U_j^{\varepsilon,n+1} - U_j^{\varepsilon,n-1}}{2k} = \frac{i\varepsilon}{4}\left(D_{xx}^s U^{\varepsilon,n+1}\Big|_{x=x_j} + S_{xx}^s U^{\varepsilon,n-1}\Big|_{x=x_j}\right) \\
&\qquad -\frac{i}{\varepsilon} f(|U_j^{\varepsilon,n}|^2) U_j^{\varepsilon,n}, \qquad j = 0, 1, \cdots, M-1, \\
&U_0^{\varepsilon,n+1} = U_M^{\varepsilon,n+1}, \qquad U_1^{\varepsilon,n+1} = U_{M+1}^{\varepsilon,n+1}, \\
&U_j^{\varepsilon,0} = U_j^{\varepsilon,1} = u_0^\varepsilon(x_j), \qquad j = 0, 1, 2, \cdots, M-1.
\end{aligned} \tag{3.24}$$

Here D_{xx}^s and S_{xx}^s are the spectral approximation and smoothed spectral approximation respectively for ∂_{xx}:

$$D_{xx}^s U|_{x=x_j} = -\frac{1}{M} \sum_{l=-M/2}^{M/2-1} \mu_l^2\, \widehat{U}_l\, e^{i\mu_l(x_j-a)}, \tag{3.25}$$

$$S_{xx}^s U|_{x=x_j} = -\frac{1}{M} \sum_{l=-M/2}^{M/2-1} \mu_l^2 r^2(l)\, \widehat{U}_l\, e^{i\mu_l(x_j-a)}, \tag{3.26}$$

with

$$r(l) = e^{-10(l/M)^{25}}.$$

In this method, the authors used the smoothed spectral approximation in the explicit terms in order to suppress aliasing instabilities for long time computations. In fact, the role of $r(l)$ is to damp the highest modes to suppress aliasing.

The schemes SP1 and SP2 are time reversible, just as the IVP for the NLS if $\tau = 0$. Also, a main advantage of the time-splitting methods is their time-transverse invariance, when $\tau = 0$ in (3.1), just as it holds for the NLS itself. If a constant α is added to the potential V, then the discrete wave functions $U_j^{\varepsilon,n+1}$ obtained from SP1 and SP2 get multiplied by the phase factor $e^{-i\alpha(n+1)k/\varepsilon}$, which leaves the discrete quadratic observables unchanged. This property does not hold for finite difference scheme, like CNSP. The schemes SP1, SP2 were analyzed for the linear Schrödinger equation ($f = 0, \tau = 0$) in the semiclassical regime in [3], where the above cited properties were shown.

Let $\mathbf{u} = (U_0, \cdots, U_{M-1})^T$ and let $\|\cdot\|_{l^2}$ be the usual discrete l^2-norm respectively on the interval (a, b), i.e.

$$\|\mathbf{u}\|_{l^2} = \sqrt{\frac{b-a}{M} \sum_{j=0}^{M-1} |U_j|^2}. \tag{3.27}$$

For the *stability* of the time-splitting spectral approximations SP1 and SP2, we cite the following lemma, which shows that the total charge is conserved.

Lemma 3.1 *The time-splitting spectral schemes (SP1) (3.16) and (SP2) (3.22) are unconditionally stable. In fact, for every mesh size $h > 0$ and time step $k > 0$,*

$$\|\mathbf{u}^{\varepsilon,n}\|_{l^2} = \|\mathbf{u}_0^{\varepsilon}\|_{l^2}, \qquad n = 1, 2, \cdots \tag{3.28}$$

Proof: Follows the line of the analogous result for the linear case in [3].

Remark 3.2 *For the linear Schrödinger equation in the semiclassical regime $0 < \varepsilon \ll 1$, it was proved in [3] that $h = O(\varepsilon)$, k independent of ε, gives convergence of the (quadratic) observables.*

4 Numerical examples

In our computations, the initial condition (1.2) is always chosen in the classical WKB form:

$$u^{\varepsilon}(\mathbf{x}, t = 0) = u_0^{\varepsilon}(\mathbf{x}) = A_0(\mathbf{x})\, e^{iS_0(\mathbf{x})/\varepsilon} = \sqrt{\rho_0(\mathbf{x})}\, e^{iS_0(\mathbf{x})/\varepsilon}, \tag{4.1}$$

with A_0 and S_0 independent of ε, real valued, regular and with $A_0(\mathbf{x})$ decaying to zero sufficiently fast as $|\mathbf{x}| \to \infty$. We always compute with SP2 on the interval $[-8, 8]$, which is large enough for the computations such that the periodic boundary conditions do not introduce a significant (aliasing) error relative to the whole space problem.

In the first two examples, analystic solutions of the semi-classical limit are available from [8] and are used for numerical comparisons.

Example 1. Weak $O(\varepsilon)$ cubic defocusing nonlinearity, i.e. in (1.1),

$$V(x) \equiv 0, \qquad f(\rho) = \varepsilon\rho, \qquad \tau = 0.$$

The initial condition is taken as

$$A_0(x) = e^{-x^2}, \qquad S_0(x) = -\frac{x^2}{2} + \varepsilon\, e^{-2x^2}\, \ln\frac{1}{\varepsilon}, \qquad x \in \mathbb{R}. \tag{4.2}$$

We choose these initial data for this example such that the weak limits of the position density ρ^ε and current density J^ε can be obtained analytically [8]. The weak limits ρ^0, J^0 of ρ^ε, J^ε respectively as $\varepsilon \to 0$, are given in [8], e.g. before breaking

$$\rho^0(x,t) = \frac{1}{1-t} e^{-2x^2/(1-t)^2}, \qquad J^0(x,t) = -\frac{x}{(1-t)^2} e^{-2x^2/(1-t)^2}, \qquad 0 \le t < 1.$$

When $t \to 1$, they are singular distributions ('δ-like'). Here we test the meshing strategy of the time-splitting spectral approximation SP2 (3.22). Figure 1 shows the numerical results at $t = 0.5$ (before breaking) with $k = 0.02$–fixed and independent of ε, and three different mesh sizes and ε's: $\mathcal{T}_0^{\varepsilon,h} = (\varepsilon_0, h_0) = (0.01, 1/128)$, $\frac{1}{4}\mathcal{T}_0^{\varepsilon,h}$, $\frac{1}{16}\mathcal{T}_0^{\varepsilon,h}$ which corresponds to the meshing strategy: $h = O(\varepsilon)$ and k independent of ε. We also output the solutions at $t = 1.5$ (after breaking) with $\mathcal{T}_0^{\varepsilon,h,k} = (\varepsilon_0, h_0, k_0) = (0.01, 1/128, 0.005)$, $\frac{1}{4}\mathcal{T}_0^{\varepsilon,h,k}$, $\frac{1}{16}\mathcal{T}_0^{\varepsilon,h,k}$ which corresponds to the meshing strategy: $h = O(\varepsilon)$ and $k = O(\varepsilon)$; and $k = 0.02$–fixed, $\mathcal{T}_0^{\varepsilon,h} = (\varepsilon_0, h_0) = (0.04, 1/32)$, $\frac{1}{4}\mathcal{T}_0^{\varepsilon,h}$, $\frac{1}{16}\mathcal{T}_0^{\varepsilon,h}$ which corresponds to the meshing strategy: $h = O(\varepsilon)$ and k independent of ε. In order to get a better visualization in this figure and the following, we depict the solution in a subinterval instead of the whole computational interval. In this figure and the following, if a type of line, e.g. '- - - ' or '. . .', is not visible from the figure, then it coincides with the solid line.

These experiments suggest that, for weak $O(\varepsilon)$ cubic defocusing nonlinearity, the SP2 or SP1 gives very accurate results in the semiclassical regime under the meshing strategy: k independent of ε, $h = O(\varepsilon)$ before breaking and $h = O(\varepsilon)$, $k = O(\varepsilon)$ after breaking.

Example 2. Weak $O(\varepsilon^{3/2})$ cubic defocusing nonlinearity, with

$$V(x) \equiv 0, \qquad f(\rho) = \varepsilon^{3/2}\rho^{3/2}, \qquad \tau = 0.$$

The initial condition is taken as

$$A_0(x) = e^{-x^2}, \qquad S_0(x) = -\frac{x^2}{2}, \qquad x \in \mathbb{R}. \tag{4.3}$$

The initial data is chosen from [8] where the semi-classical limits of the position density ρ^ε and current density J^ε are given analytically. Introduce the Wigner transform

$$W^\varepsilon(u^\varepsilon)(x,\xi,t) = \frac{1}{2\pi}\int u^\varepsilon\left(x - \frac{\varepsilon v}{2}, t\right) \bar{u}^\varepsilon\left(x + \frac{\varepsilon v}{2}, t\right) e^{i\xi v}\, dv, \tag{4.4}$$

(cf. [13, 15, 27, 8]). The Wigner measure (i.e. the weak limit of $W^\varepsilon(u^\varepsilon)$ as $\varepsilon \to 0+$) of this problem is given in [8]:

$$\mu(x,\xi,t) = \begin{cases} \frac{1}{1-t}\left|A_0\left(\frac{x}{1-t}\right)\right|^2 dx \otimes \delta\left(\xi - \frac{x}{t-1}\right), & t < 1, \\ \frac{1}{t-1}\left|\mathcal{Z}A_0\left(\frac{x}{1-t}\right)\right|^2 dx \otimes \delta\left(\xi - \frac{x}{t-1}\right), & t > 1; \end{cases}$$

where the operator $\mathcal{Z}$ is related to the scattering operator [8]. From the above formula we know that for fixed t, the "peak" of the Wigner function is the line $\xi = \frac{x}{t-1}$ in the $x-\xi$ plane. The weak limits ρ^0, J^0 of ρ^ε, J^ε respectively as $\varepsilon \to 0$, are the zeroth and first moments of μ, respectively.

As a post-processing we compute numerically the Wigner-function corresponding to the wave-function obtained by SP2. After obtaining the solution of the nonlinear Schödinger equation (3.1), we compute the Wigner function via (4.4) by using the composite trapezoidal quadrature formula on a very fine grid of an interval in the v-axis for each fixed (x,ξ). Here we also test the meshing strategy of SP2. Figure 2 shows the surface plot and contour plot of $W^\varepsilon(u^\varepsilon)(x,\xi,t)$ for $\varepsilon = 0.04$ at $t = 0.5$ (before breaking, peak line at $\xi = -2x$), $t = 1.0$ (peak line at $x = 0$) and $t = 1.5$ (after breaking, peak line at $\xi = 2x$). Furthermore Figure 3 shows the results at $t = 0.5$ (before breaking) with $k = 0.02$-independent of ε when we choose $\mathcal{T}_0^{\varepsilon,h} = (0.04, 1/32)$, $\frac{1}{4}\mathcal{T}_0^{\varepsilon,h}$, $\frac{1}{16}\mathcal{T}_0^{\varepsilon,h}$ corresponding to the meshing strategy: $h = O(\varepsilon)$ and k independent of ε, and $t = 1.5$ (after breaking) when we choose $\mathcal{T}_0^{\varepsilon,h,k} = (0.01, 1/128, 0.005)$, $\frac{1}{4}\mathcal{T}_0^{\varepsilon,h,k}$, $\frac{1}{16}\mathcal{T}_0^{\varepsilon,h,k}$ which corresponds to the meshing strategy: $h = O(\varepsilon)$ and $k = O(\varepsilon)$; and finally the same set of parameters for ε and h ($h = O(\varepsilon)$) with $k = 0.02$ fixed and independent of ε.

From Figure 2 we can see that the peak line of the numerical Wigner function is at the exact position and moves at the correct speed of the analytic solution. Figure 3 indicates that the same meshing strategy is required for the weak $O(\varepsilon^{3/2})$ defocusing nonlinearity as for the weak $O(\varepsilon)$ nonlinearity.

Example 3. Strong $O(1)$ cubic defocusing nonlinearity,

$$V(x) \equiv 0, \qquad f(\rho) = \rho, \qquad \tau = 0.$$

The initial condition is taken as

$$A_0(x) = \begin{cases} 1 - |x|, & |x| < 1, \\ 0, & \text{otherwise;} \end{cases} \qquad S_0(x) = -\ln(e^x + e^{-x}), \quad x \in \mathbb{R}. \tag{4.5}$$

This initial data is not analytic at $x = 0$ and $x = \pm 1$. For numerical study of NLS with cubic defocusing nonlinearity and analytic initial data, we refer [3, 20, 28, 29]. To test the numerical method, for each fixed ε, we compute the numerical solution with a very fine mesh, e.g. $h = \frac{1}{4096}$, and a very small time step, e.g. $k = 0.00001$, as the reference 'exact' solution u^ε. Figure 4 shows the numerical results at $t = 0.5$ with $\mathcal{T}_0^{\varepsilon,h,k} = (0.04, 1/32, 0.01)$, $\frac{1}{4}\mathcal{T}_0^{\varepsilon,h,k}$, $\frac{1}{16}\mathcal{T}_0^{\varepsilon,h,k}$ corresponding to the meshing strategy

$h = O(\varepsilon)$ and $k = O(\varepsilon)$; and the results by choosing $k = 0.01$ fixed, $\mathcal{T}_0^{\varepsilon,h} = (0.04, 1/32)$, $\frac{1}{4}\mathcal{T}_0^{\varepsilon,h}$, $\frac{1}{16}\mathcal{T}_0^{\varepsilon,h}$ which corresponds to the meshing strategy $h = O(\varepsilon)$ and k independent of ε. In Figure 5 we show $\rho = |u^\varepsilon|^2$ in space-time for $\varepsilon = 0.0025$.

To verify the weak convergence (in the x-variable) of ρ^ε as $\varepsilon \to 0$, we compute the integral

$$\int_{-\infty}^{x} \rho^\varepsilon(s,t)\, ds, \tag{4.6}$$

for various ε's. Figure 6 displays this integral (using the reference 'exact' solution) at $t = 0.5$ for three different values of ε: 0.04, 0.01 and 0.0025. Figure 6 clearly demonstrates the strong convergence of the position density integral as ε goes to zero.

Example 4. Weak $O(\varepsilon)$ cubic focusing nonlinearity,

$$V(x) \equiv 0, \qquad f(\rho) = -\varepsilon\rho, \qquad \tau = 0.$$

The initial condition is taken as

$$A_0(x) = e^{-x^2}, \qquad S_0(x) = -\ln(e^x + e^{-x}), \qquad x \in \mathbb{R}. \tag{4.7}$$

This set of compressional initial data was widely used for numerical study of the semi-classical limits of linear Schrödinger equation [3, 28, 29] and NLS with cubic defocusing nonlinearity [3, 28, 29, 20]. Here we use it for NLS with weak $O(\varepsilon)$ cubic focusing nonlinearity. The reference "exact" solution u^ε is obtained in the same way as in Example 3. Figure 7 shows the numerical results at $t = 1.5$ with $\mathcal{T}_0^{\varepsilon,h,k} = (0.04, 1/32, 0.02)$, $\frac{1}{4}\mathcal{T}_0^{\varepsilon,h,k}$, $\frac{1}{16}\mathcal{T}_0^{\varepsilon,h,k}$ which corresponds to the meshing strategy $h = O(\varepsilon)$ and $k = O(\varepsilon)$; and the solutions by choosing $k = 0.02$ fixed, $\mathcal{T}_0^{\varepsilon,h} = (0.04, 1/32)$, $\frac{1}{4}\mathcal{T}_0^{\varepsilon,h}$, $\frac{1}{16}\mathcal{T}_0^{\varepsilon,h}$ which corresponds to the meshing strategy: $h = O(\varepsilon)$ and k independent of ε. Figure 8 plots $\rho = |u^\varepsilon|^2$ in space-time for $\varepsilon = 0.0025$. Figure 9 shows the position density integral (4.6) at $t = 1.5$ for four different values of ε: 0.04, 0.01, 0.0025 and 0.000625.

Figures 1, 3, 5 and 7 seem to suggest the following meshing strategy in order to guarantee good approximations of observables for defocusing nonlinearities and weak $O(\varepsilon)$ focusing nonlinearities:

$$h = O(\varepsilon), \qquad k = O(\varepsilon). \tag{4.8}$$

A weaker constraint on the meshing, e.g. $h = O(\varepsilon)$ and k independent of ε, gives incorrect numerical observables.

Example 5. Strong $O(1)$ cubic focusing nonlinearity:

$$V(x) \equiv 0, \qquad f(\rho) = -\rho, \qquad \tau = 0.$$

We present computations for two types of initial values A_0 and S_0:

I. Zero initial phase data

$$A_0(x) = e^{-x^2}, \qquad S_0(x) = 0, \qquad x \in \mathbb{R}; \tag{4.9}$$

II. Symmetric initial data with nonzero phase

$$A_0(x) = e^{-x^2}, \qquad S_0(x) = \frac{1}{e^x + e^{-x}}, \qquad x \in \mathbb{R}. \tag{4.10}$$

These sets of initial data were already used in [9] for numerical study of the semi-classical limits of NLS with cubic focusing nonlinearity by using a different numerical method. Here we use them to study our numerical method SP2. In fact, the initial data is very similar to the pure soliton data studied by Miller and Kamvissis [30]: $A_0(x) = 2\mathrm{sech}(x)$, $S_0(x) = 0$. For Miller and Kamvissis's data, the Zakharov-Shabat operator has pure imaginary eigenvalues and the reflection coefficients are exactly zero. For our data set I: the eigenvalues are almost pure imaginary and the reflcetion coefficients are exponentially small for small ε; for set II: the eigenvalues are symmetric about the pure imaginary axis, and are located roughly on a convex "parabola" whose vertex is at the origin [9, 7]. They illustrate the main numerical difficulties and qualitative phenomena for the focusing nonlinear Schrödinger equation. The reference 'exact' solution u^ε is obtained in the same way as in the Example 3. One see "seas of solitons" after the formation of caustics. Figures 10-12 show $\rho^\varepsilon = |u^\varepsilon|^2$ in space-time with zero initial phase data and $\varepsilon = 0.1, 0.05$ and 0.025, respectively. Figure 13 shows the position density integral (4.6) at $t = 1.2$ for five different ε's: 0.1, 0.05, 0.025, 0.0125 and 0.00625.

To compare SP2 with the CNSP, in Figure 14 we show the numerical density ρ^ε for zero initial phase data at $t = 0.8$ and $t = 1.2$ obtained by the two methods with $\mathcal{T}_0^{\varepsilon,h} = (0.2, 1/32)$ and $k_0 = 0.01$, $\frac{1}{2}\mathcal{T}_0^{\varepsilon,h}$ and $\frac{1}{4}k_0$, $\frac{1}{4}\mathcal{T}_0^{\varepsilon,h}$ and $\frac{1}{40}k_0$, which corresponds to the meshing strategy: $h = O(\varepsilon)$ and $k = o(\varepsilon)$.

In Figure 15 we show $\rho^\varepsilon = |u^\varepsilon|^2$ in space-time for the nonzero initial phase data for $\varepsilon = 0.025$. Figure 16 shows the indefinite integral at $t = 1.0$ for $\varepsilon = 0.05$, 0.025, 0.0125 and 0.00625. Figure 17 shows the comparison between SP2 and CNSP for the nonzero initial phase data. Figure 18 depicts the densities at $t = 0.2$, 0.3, 0.4 for $\varepsilon = 0.0125$ and the nonzero initial phase data obtained by SP2 with and without the Krasny filter.

Figures 14 and 17 show that SP2 gives much better density approximations than those obtained by the CNSP using the same mesh size and time step. Figure 18 shows that, for the strong $O(1)$ focusing nonlinearity the Krasny filter is needed for small ε in order to obtain the correct solution to longer times. In fact, the solution obtained by SP2 without the filter is not even with respect to $x = 0$ while the correct solution is an even function. This was due to the round-off error which is an issue of concern for physically unstable problems. Our numerical experiment indicates the following meshing strategy for strong $O(1)$ focusing nonlinearity (using Krasny's filter):

$$h = O(\varepsilon), \qquad k = o(\varepsilon).$$

Example 6. Cubic nonlinearity with confining potential:

$$V(x) = \frac{\omega x^2}{2}, \qquad f(\rho) = \beta\rho, \qquad \tau = 0.$$

This is the Gross-Pitaevskii equation (GPE) related to Bose-Einstein condensation (BEC), see [12]. For the physical background and mathematical model of BEC, we refer [18, 31, 1, 2] and for a systematic numerical study of GPE in terms of BEC see [5, 6, 4]. BEC occurs when interacting trapped bosons are cooled down to a temperature below the critical one. Then the particles fall into the same quantum mechanical ground state. The GPE describes the evolution of this ground state due to, say, a change in the trap frequencies. Here we only report sample computation for the GPE, where we chose the following initial condition (non-ground state!):

$$A_0(x) = e^{-x^2}, \qquad S_0(x) = -\ln(e^x + e^{-x}), \qquad x \in \mathbb{R}. \tag{4.11}$$

Figure 19 shows the density $\rho^\varepsilon = |u^\varepsilon|^2$ of the solutions in space-time for the defocusing nonlinearity, i.e. $\beta = 1$, with $\varepsilon = 0.01$ for different ω. Figure 20 shows similar results for the focusing nonlinearity, i.e. $\beta = -1$ with $\varepsilon = 0.025$ for different ω's.

Figures 19 and 20 illustrate the fact that the confinement becomes stronger as ω increases.

Example 7. A comparison between the solution of the NLS (3.1) and its hydrodynamical limit (2.7), (2.8) in the defocusing case,

$$V(x) = 0.0, \qquad f(\rho) = \frac{\gamma}{\gamma - 1}\rho^{\gamma - 1}.$$

Accordingly, in (2.6),

$$P(\rho) = \rho^\gamma, \qquad \gamma > 1.$$

The initial condition is taken as

$$A_0(x) = e^{-x^2}, \qquad S_0(x) = \frac{1}{e^{3x} + e^{-3x}}, \qquad x \in \mathbb{R}. \tag{4.12}$$

The system (2.7)-(2.8) is solved by the second-order relaxed scheme [21]. Figure 21 shows the solutions of the Schrödinger equation (3.1) and (2.7), (2.8) at different times with different values of γ and τ. In this figure, 'SHDE' represents the solution of the hydrodynamic equations (2.7), (2.8), while the other lines represent the solution of the Schrödinger equation with various values of ε. Figure 22 shows $\rho^\varepsilon = |u^\varepsilon|^2$ in space-time with $\gamma = 1.4$ and $\varepsilon = 0.01$ for different values of τ.

Figure 21 indicates that, when the solution of (2.7), (2.8) is smooth (no caustics, i.e. before breaking), the first two observables of the solution of the Schrödinger equation (1.1) converge to the solution of the formal hydrodynamic limit when $\varepsilon \to 0$. On the contrary, when a shock appears in the solution of (2.7), (2.8), its location and speed are different from that of the Schrödinger equation. One also sees that the larger τ, the later the shock appears. Furthermore when τ is sufficiently large, i.e. with a sufficiently small relaxation time, no shock appears in the solution of (2.7), (2.8) (on the computed interval).

5 Conclusions

Time-splitting spectral approximations for the nonlinear Schrödinger equation in the semiclassical regimes (i.e. for small scaled Planck constant ε) were studied. The discretization method is a time-splitting method with the Fourier spectral approximation of the spatial derivative. This method conserves the total charge, is time reversible, time-transverse invariant when the corresponding Schrödinger equation is, and is very effective in capturing oscillatory solutions of the NLS for small ε.

Our numerical study suggests the following meshing strategies for obtaining the 'correct' observables: $k = O(\varepsilon)$ and $h = O(\varepsilon)$ for defocusing nonlinearities and weak $O(\varepsilon)$ focusing nonlinearities; $k = o(\varepsilon)$ and $h = O(\varepsilon)$ for strong $O(1)$ focusing nonlinearities. Numerical results for the NLS related to Bose-Einstein condensation are also presented. Furthermore comparisons between the solution of the nonlinear Schrödinger equation and its formal semiclassical limit (hydrodynamic equations) are presented. Before shocks appear, the observables of the solution of the Schrödinger equation converge to the solution of its semiclassical limit (Euler system) when the (scaled) Planck constant $\varepsilon \to 0$ (cf. Grenier [17]). On the contrary, after shocks appear, the shock speeds of the Schrödinger equation and its formal semiclassical limit are different.

Acknowledgment

W.B. acknowledges support by the National University of Singapore grant No. R-151-000-016-112 and helpful discussions with Chi-Wang Shu. S.J. acknowledges support in part by NSF grant No. DMS-0196106. P.A.M. acknowledges support from the EU-funded TMR network 'Asymptotic Methods in kinetic Theory' and from his WITTGENSTEIN-AWARD 2000, funded by the Austrian National Science Fund FWF. We thank discussions with Norbert J. Mauser and Hans P. Stimming. This research was supported in part by the International Erwin Schrödinger Institute in Vienna and the START project 'Nonlinear Schrödinger and quantum Boltzmann equations' (FWF Y137-TEC) of N.J. Mauser.

References

[1] M.H. Anderson, J.R. Ensher, M.R. Matthews, C.E. Wieman, and E.A. Cornell, Observation of Bose-Einstein condensation in a dilute atomic vapor, Science, 269(1995), pp. 198-201.

[2] J.R. Anglin and W. Ketterle, Bose-Einstein condensation of atomic gases, Nature, 416(2002), pp. 211-218.

[3] W. Bao, Shi Jin and P.A. Markowich, On time-splitting spectral approximations for the Schrödinger equation in the semiclassical regime, J. Comput. Phys., 175(2002), pp. 487-524.

[4] W. Bao and W. Tang, Ground state solution of trapped interacting Bose-Einstein condensate by minimizing a functional, preprint.

[5] W. Bao, D. Jaksch and P.A. Markowich, Numerical solution of the Gross-Pitaevskii equation for Bose-Einstein condensation, preprint.

[6] W. Bao, D. Jaksch, Numerical methods for solving damped nonlinear Schrodinger equations with a focusing nonlinearity, preprint.

[7] J.C. Bronski and D. W. McLaughlin, Semiclassical behavior in the NLS equation: optical shocks - focusing instabilities, Singular Limits of Dispersive Waves, Plenum Press, New York and London, 1994.

[8] R. Carles, Remarques sur les mesures de Wigner, preprint.

[9] H.D. Ceniceros and F.R. Tian, A numerical study of the semi-classical limit of the focusing nonlinear Schrödinger equation, preprint.

[10] B. Desjardins, C.K. Lin and T.C. Tso, Semiclassical limit of the derivative nonlinear Schrödinger equation, M^3AS, 10(2000), pp. 261-285.

[11] A. Fannjiang, Shi Jin and G. Papanicolaou, High frequency behavior of the focusing nonlinear Schrödinger equation with random inhomogeneities, SIAM J. Appl. Math., to appear.

[12] S.A. Gardiner, D. Jaksch, R. Dum, J.I. Cirac and P. Zollar, Nonlinear matter wave dynamics with a chaotic potential, Phys. Rev. A, 62(2000), pp. 023612-1:21.

[13] I. Gasser and P.A. Markowich, Quantum hydrodynamics, Wigner transforms and the classical limit, Asymptotic Analysis, 14(1997), pp. 97-116.

[14] P. Gérard, Microlocal defect measures, Comm. PDE., 16(1991), pp. 1761-1794.

[15] P. Gérard, P.A. Markowich, N.J. Mauser and F. Poupaud, Homogenization limits and Wigner transforms, Comm. Pure Appl. Math., 50(1997), pp. 321-377.

[16] D. Gottlieb and S.A. Orszag, Numerical Analysis of Spectral Methods, SIAM, Philadelphia, 1977.

[17] E. Grenier, Semiclassical limit of the nonlinear Schrödinger equation in small time, Proc. Amer. Math. Soc., 126(1998), pp. 523-530.

[18] E.P. Gross, Nuovo. Cimento., 20(1961), pp. 454.

[19] Shan Jin, C.D. Levermore and D. W. McLaughlin, The semiclassical limit of the defocusing NLS hierarchy, Comm. Pure Appl. Math., LII(1999), pp. 613-654.

[20] Shan Jin, C.D. Levermore and D. W. McLaughlin, The behavior of solutions of the NLS equation in the semiclassical limit, Singular Limits of Dispersive Waves, Plenum Press, New York and London, 1994.

[21] Shi Jin and Z.P. Xin, The relaxation schemes for systems of conservation laws in arbitrary space dimensions, Comm. Pure Appl. Math., 48(1995), pp. 235-276.

[22] A. Jüngel, Nonlinear problems in quantum semiconductor modeling, Nonlin. Anal., Proceedings of WCNA2000, to appear.

[23] A. Jüngel, Quasi-hydrodynamic semiconductor equations, Progress in Nonlinear Differential Equations and Its Applications, Birkhäuser, Basel, 2001.

[24] R. Krasny, A study of singularity formulation in a vortex sheet by the point-vortex approximation, J. Fluid Mech., 167(1986), pp. 65-93.

[25] Laudau and Lifschitz, Quantum Mechanics: Non-Relativistic Theory, Pergamon Press, New York, 1977.

[26] C.K. Lin and H. Li, Semiclassical limit and well-posedness of Schödinger-Poisson and quantum hydrodynamics, preprint.

[27] P.A. Markowich, N.J. Mauser and F. Poupaud, A Wigner function approach to semiclassical limits: electrons in a periodic potential, J. Math. Phys., 35(1994), pp. 1066-1094.

[28] P.A. Markowich, P. Pietra and C. Pohl, Numerical approximation of quadratic observables of Schrödinger-type equations in the semi-classical limit, Numer. Math., 81(1999), pp. 595-630.

[29] P.A. Markowich, P. Pietra, C. Pohl and H.P. Stimming, A Wigner-Measure Analysis of the Dufort-Frankel scheme for the Schrödinger equation, preprint.

[30] P.D. Miller, S. Kamvissis, On the semiclassical limit of the focusing nonlinear Schrödinger equation, Phys. Letters A, 247(1998), pp. 75-86.

[31] L.P. Pitaevskii, Zh. Eksp. Teor. Fiz., 40(1961), pp. 646. (Sov. Phys. JETP, 13(1961), pp. 451).

[32] D. Pathria and J.L. Morris, Pseudo-spectral solution of nonlinear Schrödinger equation, J. Comput. Phys., 87(1980), pp. 108-125.

[33] L. Tartar, H-measures: a new approach for studying homogenization, oscillations and concentration effects in partial differential equations, Proc. Roy. Soc. Edinburgh Sect. A, 115(1990), pp. 193-230.

position density current density

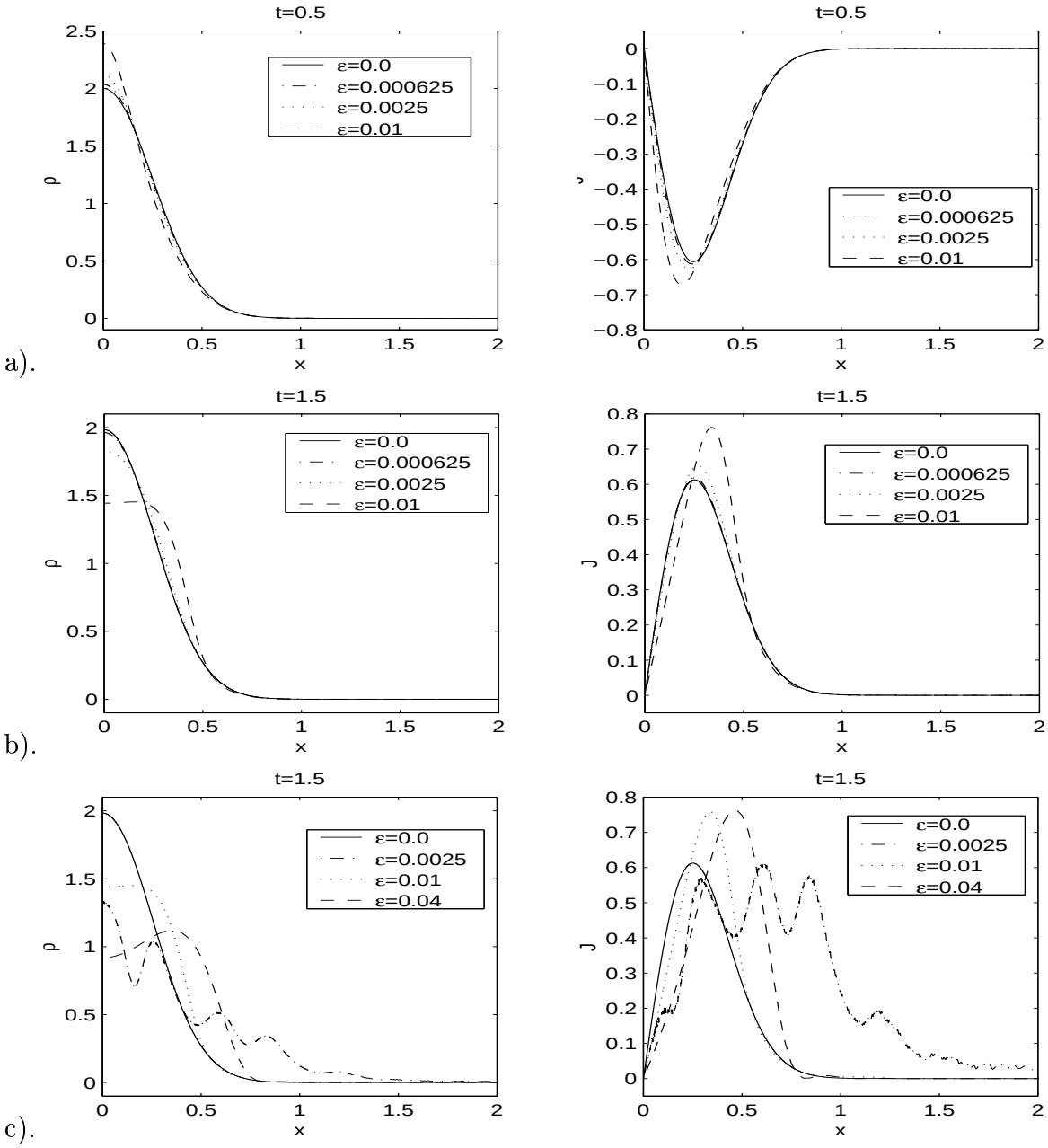

Figure 1: Numerical solutions of Example 1 by SP2 for the weak $O(\varepsilon)$ defocusing nonlinearlity. $V(x) \equiv 0$, $f(\rho) = \varepsilon\,\rho$, $\tau = 0.0$. a). At $t = 0.5$ (before breaking) under the meshing strategy: $h = O(\varepsilon)$, $k = 0.02$-independent of ε, b). At $t = 1.5$ (after breaking) under: $h = O(\varepsilon)$, $k = O(\varepsilon)$, c). At $t = 1.5$ under: $h = O(\varepsilon)$, $k = 0.02$ (independent of ε).

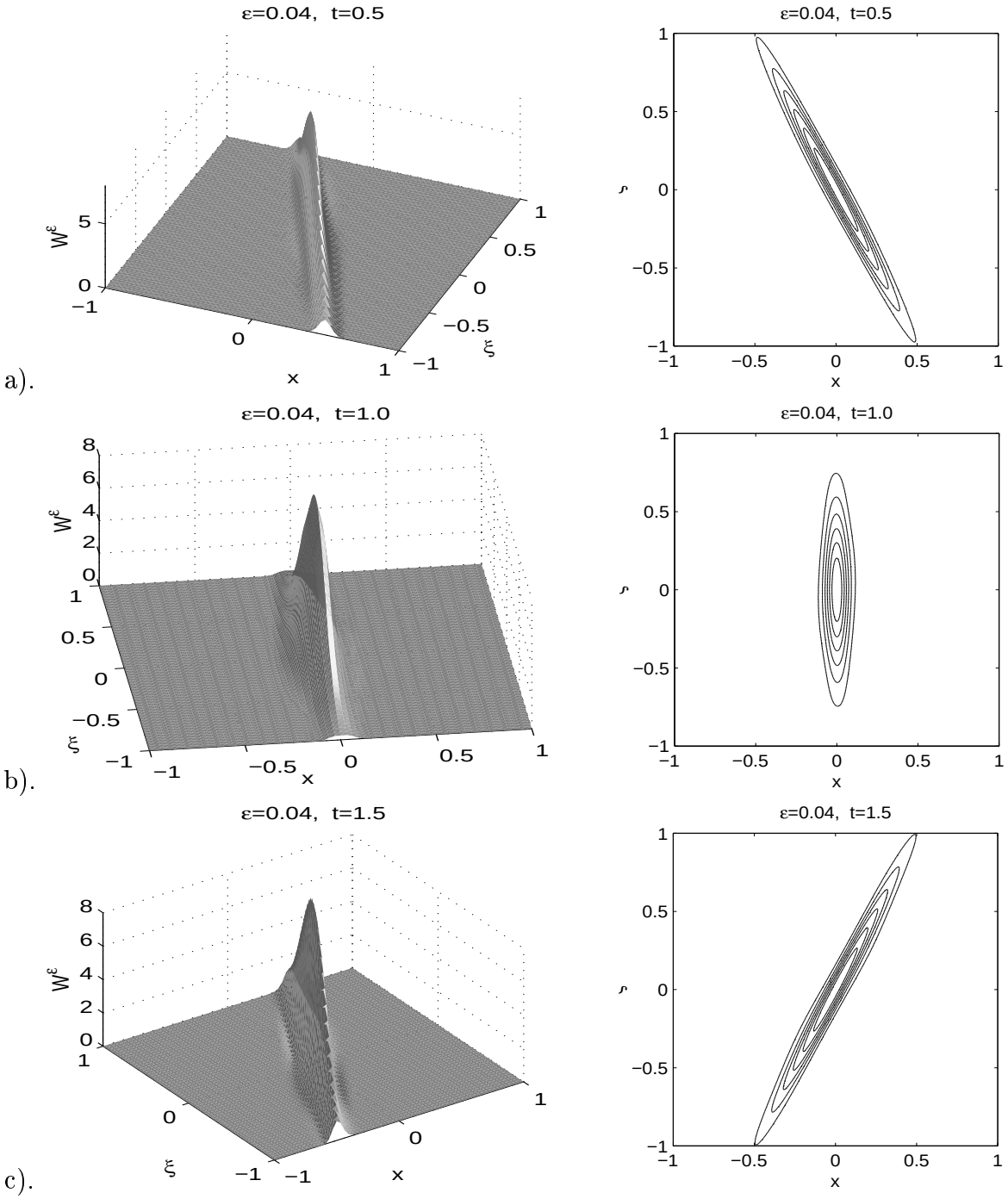

a).

b).

c).

Figure 2: Surface plot and contour plot of the Wigner function by SP2 in Example 2 for the weak $O(\varepsilon^{3/2})$ defocusing nonlinearity by using SP2. $V(x) \equiv 0$, $f(\rho) = \varepsilon^{3/2}\,\rho^{3/2}$, $\tau = 0.0$. $\varepsilon = 0.04$, $h = \frac{1}{32}$, $k = 0.02$. Left: surface-plot; right: contour-plot. a). $t = 0.5$, b). $t = 1.0$, c). $t = 1.5$

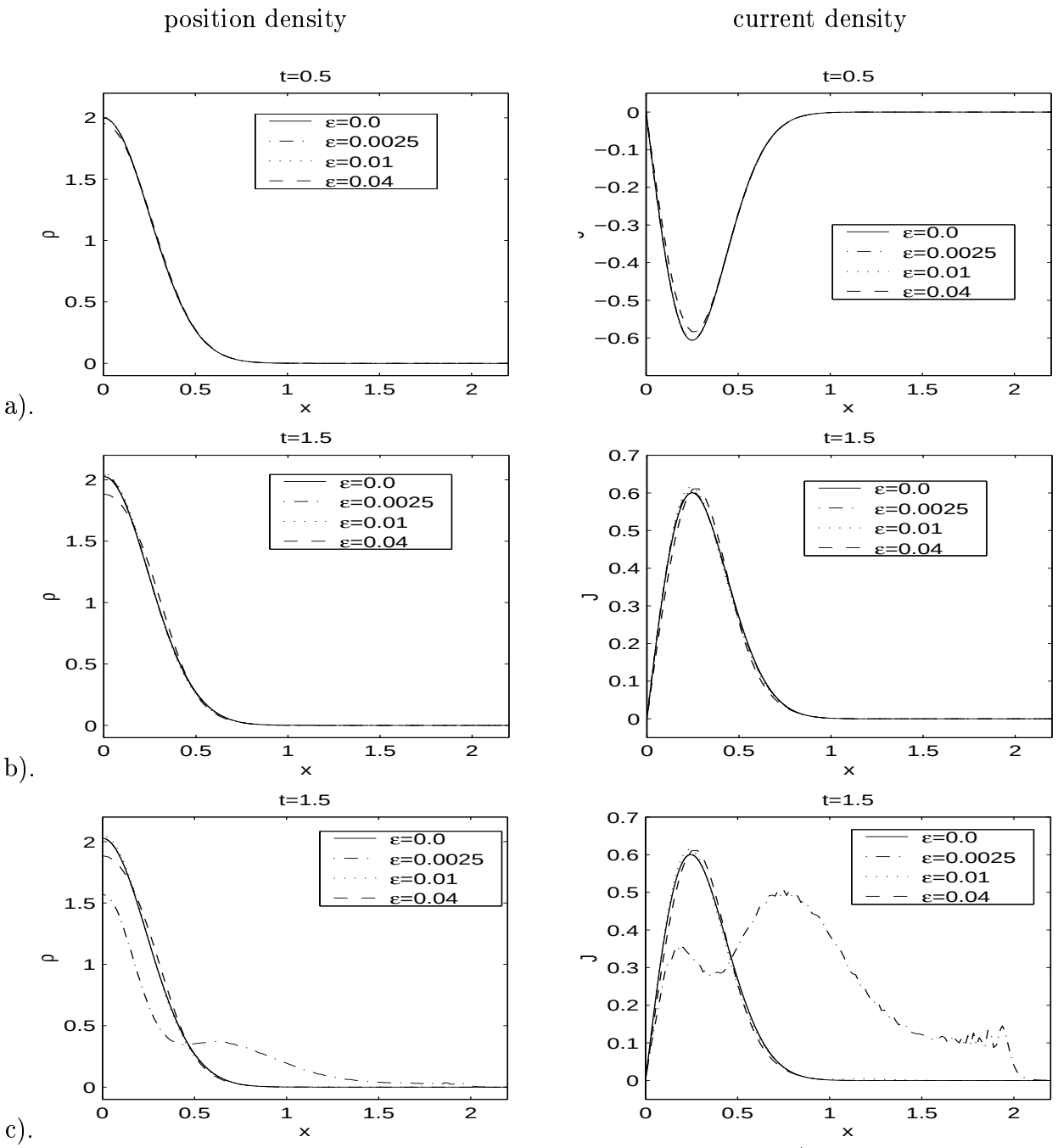

Figure 3: Numerical solutions in Example 2 for the weak $O(\varepsilon^{3/2})$ defocusing nonlinearity by using SP2. $V(x) \equiv 0$, $f(\rho) = \varepsilon^{3/2}\rho^{3/2}$, $\tau = 0.0$. a). At $t = 0.5$ (before breaking) under: $h = O(\varepsilon)$, $k = 0.02$-independent of ε, b). At $t = 1.5$ (after breaking) under: $h = O(\varepsilon)$, $k = O(\varepsilon)$, c). At $t = 1.5$ under: $h = O(\varepsilon)$, $k = 0.02$-independent of ε. In this figure and the following, if a type of line, e.g. '- - - ', is not visible from the figure, it means that it coincides with the solid line.

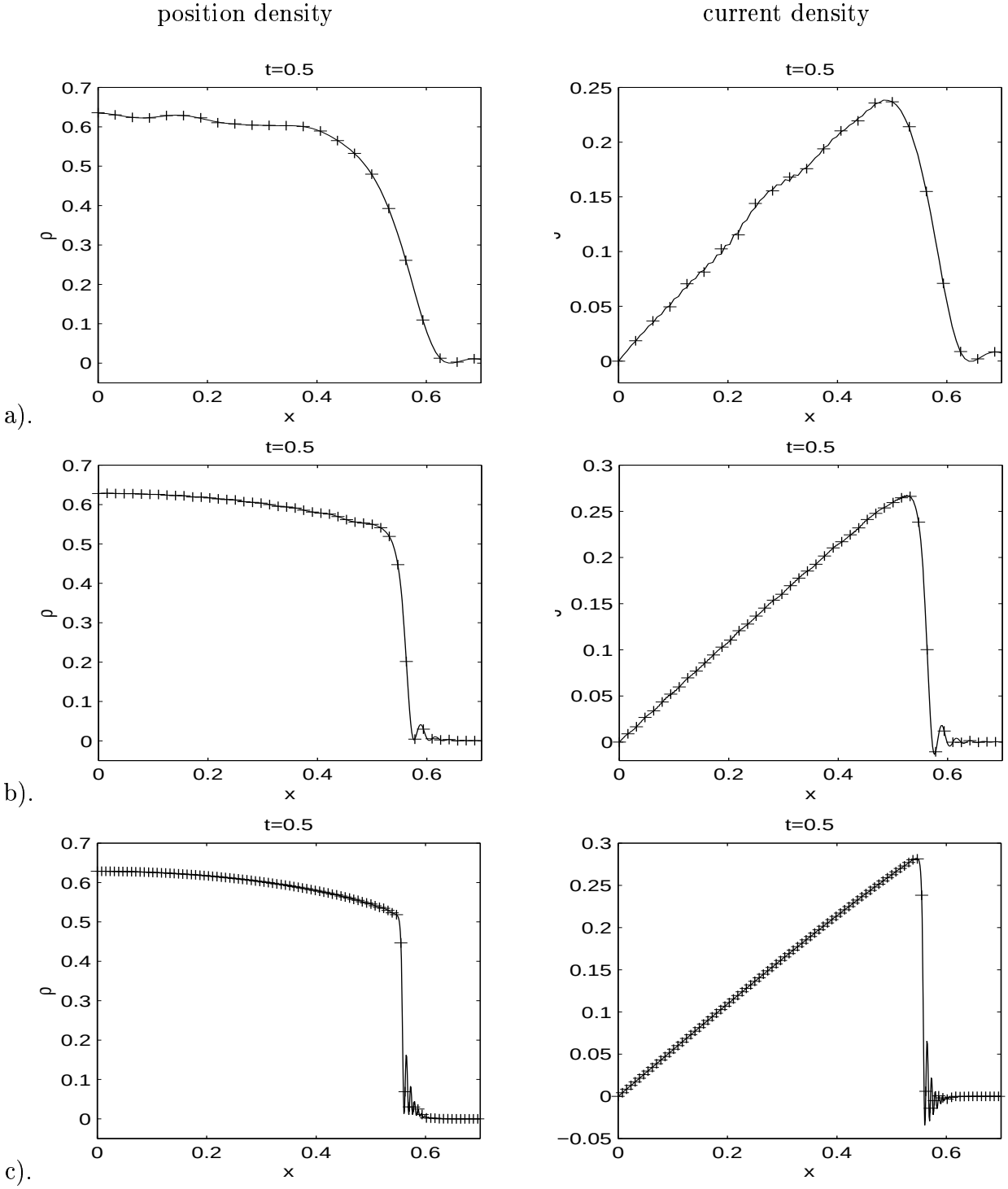

Figure 4: Numerical solutions at $t = 0.5$ in Example 3 for the strong $O(1)$ defocusing nonlinearity by using SP2. $V(x) \equiv 0$, $f(\rho) = \rho$, $\tau = 0$. '—': 'exact' solution', '+ + +': numerical solution. a). $\mathcal{T}_0^{\varepsilon,h,k} = (0.04, 1/32, 0.01)$, b). $\frac{1}{4}\mathcal{T}_0^{\varepsilon,h,k}$,). $\frac{1}{16}\mathcal{T}_0^{\varepsilon,h,k}$. Here $h = O(\varepsilon), k = O(\varepsilon)$.

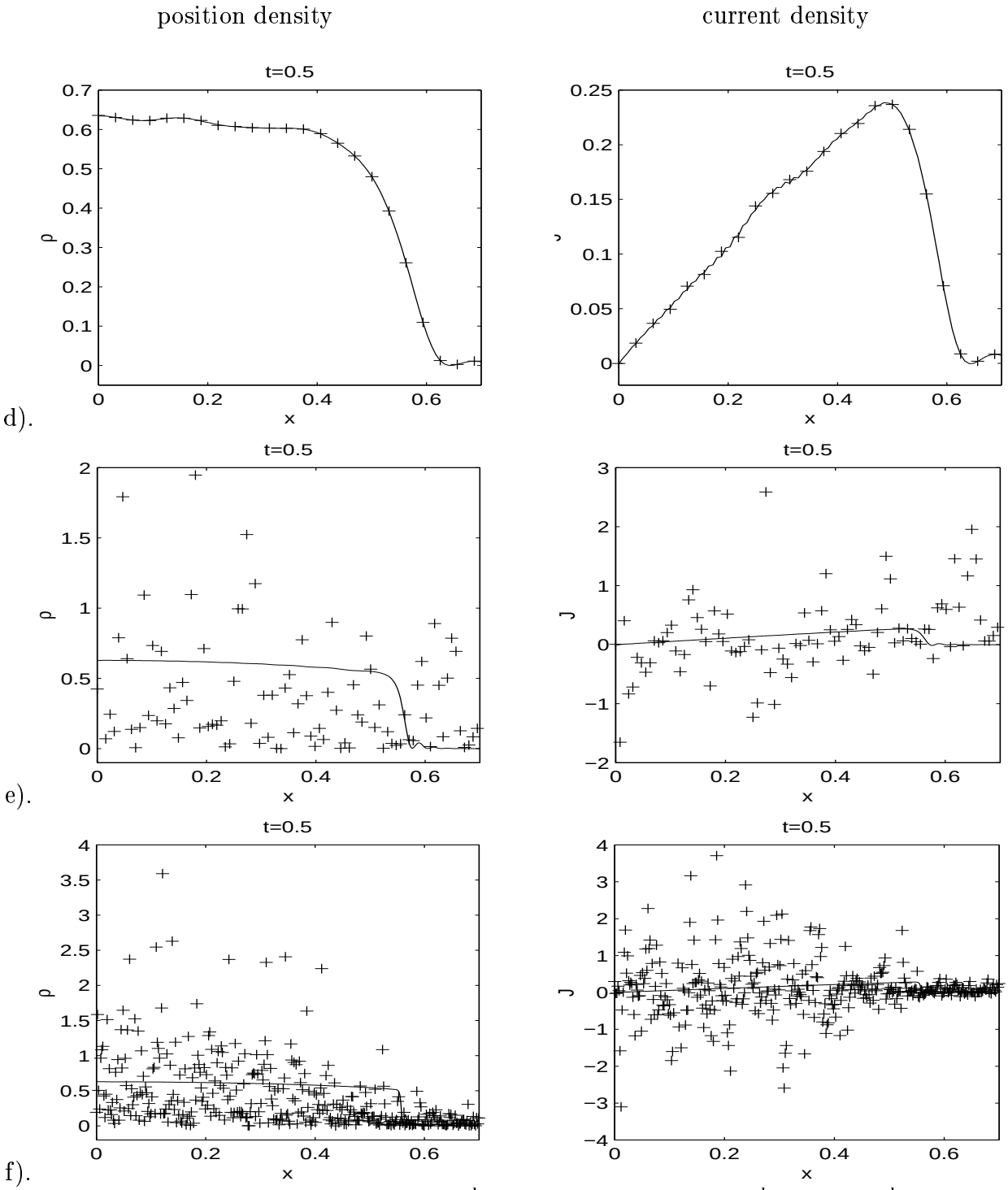

Figure 4 (cont'd). $k = 0.01$. d). $\mathcal{T}_0^{\varepsilon,h} = (0.04, 1/32)$, e). $\frac{1}{4}\mathcal{T}_0^{\varepsilon,h}$, f). $\frac{1}{16}\mathcal{T}_0^{\varepsilon,h}$. Here $h = O(\varepsilon)$, k is independent of ε.

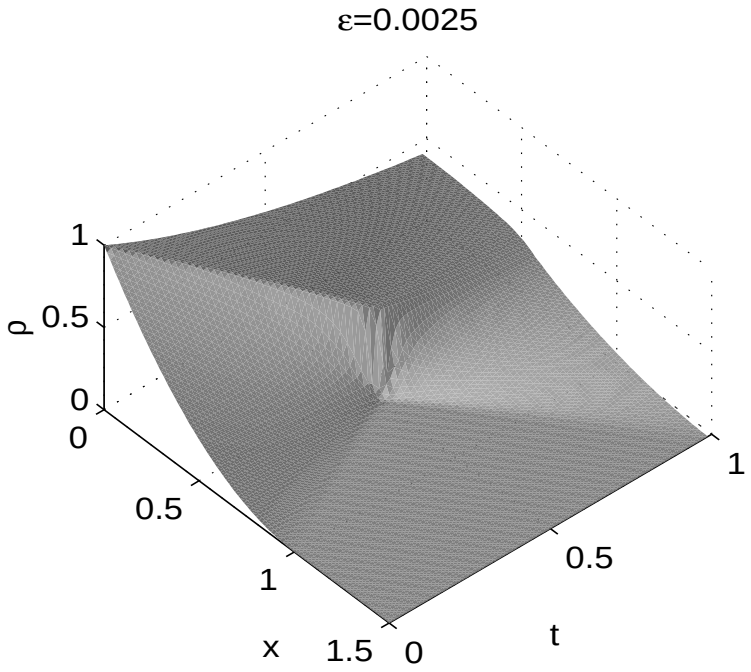

Figure 5: Evolution of the position density in Example 3 for $\varepsilon = 0.0025$.

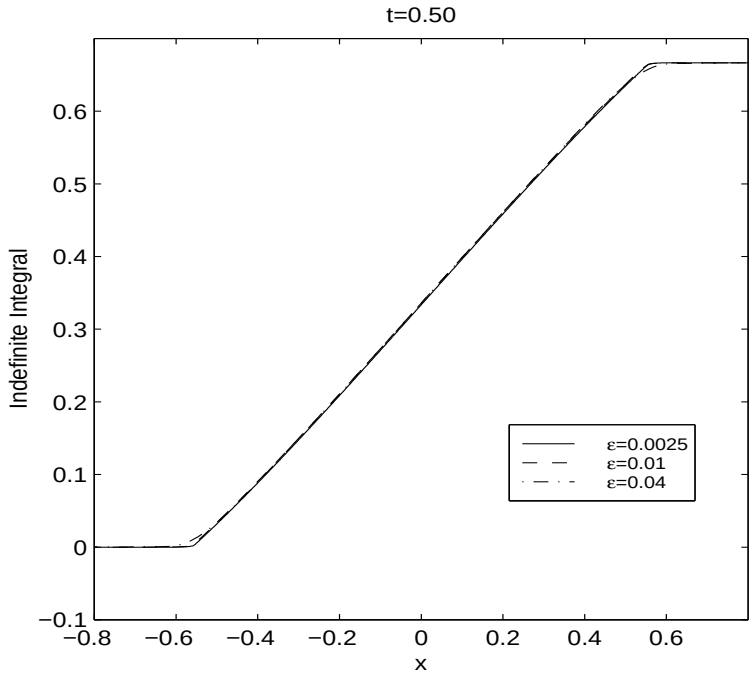

Figure 6: Indefinite integrals of the density $\rho^{\varepsilon}(x, t = 0.5)$ in Example 3 illustrating weak convergence.

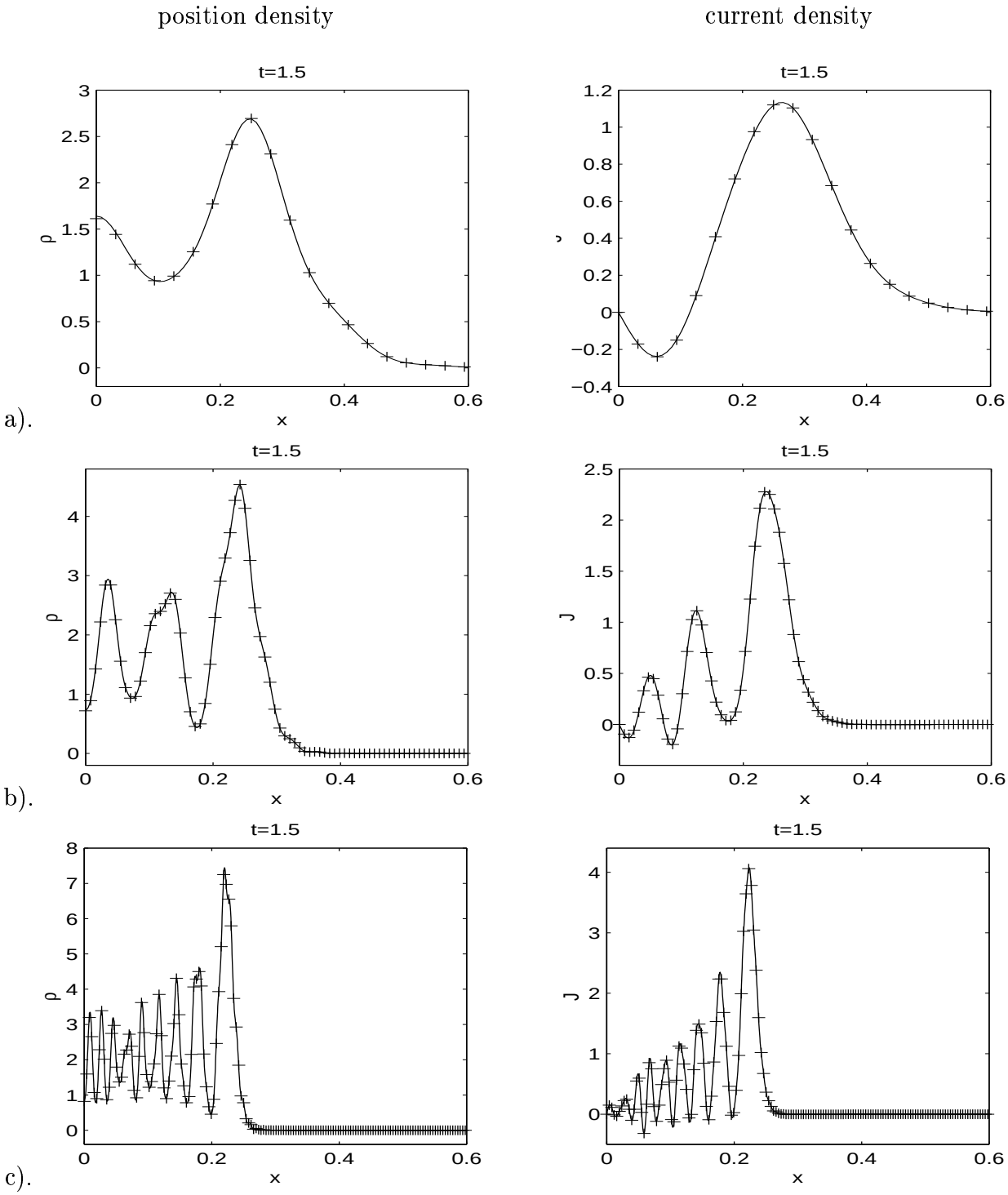

Figure 7: Numerical solutions at $t = 1.5$ in Example 4 for the weak $O(\varepsilon)$ focusing nonlinearity by using SP2. $V(x) \equiv 0$, $f(\rho) = -\varepsilon\,\rho$, $\tau = 0$. '—': 'exact' solution', '+ + +': numerical solution. a). $\mathcal{T}_0^{\varepsilon,h,k} = (0.04, 1/32, 0.02)$, b). $\frac{1}{4}\mathcal{T}_0^{\varepsilon,h,k}$, c). $\frac{1}{16}\mathcal{T}_0^{\varepsilon,h,k}$. Here $h = O(\varepsilon), k = O(\varepsilon)$.

position density

current density

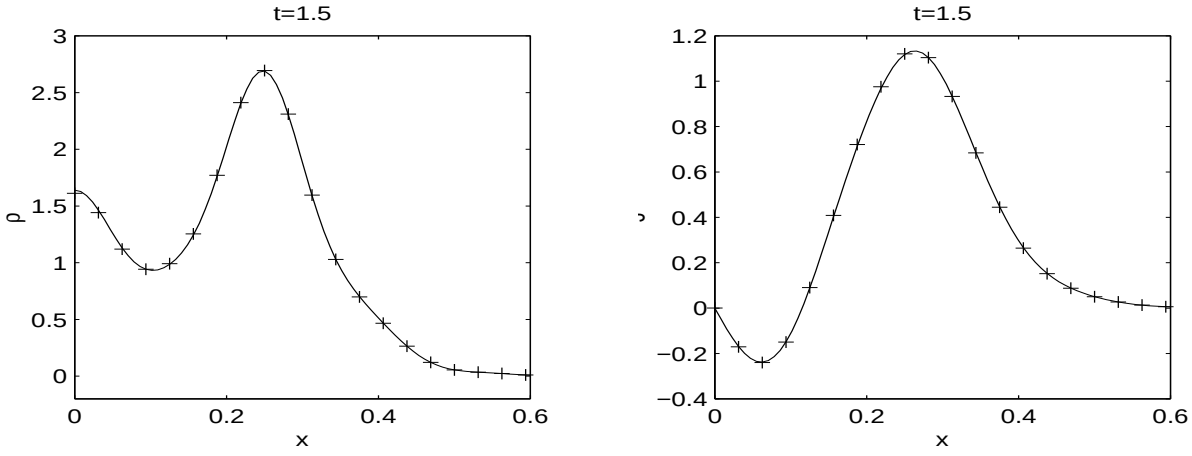

d).

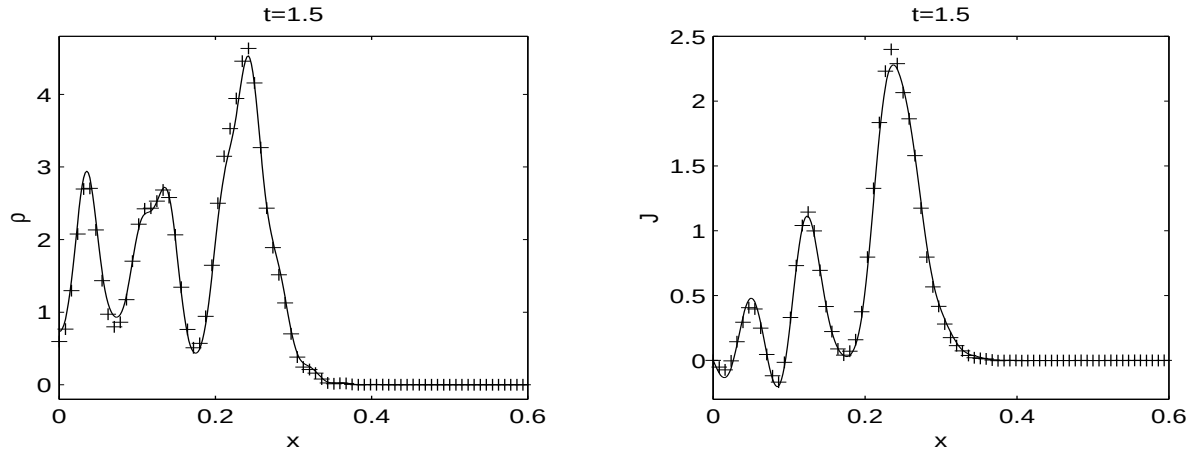

e).

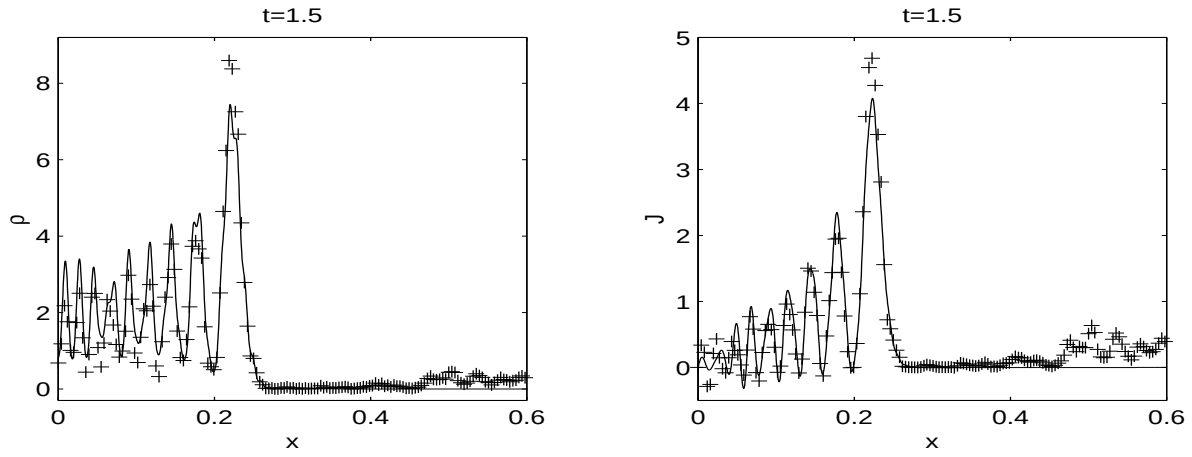

f).

Figure 7 (cont'd). $k = 0.02$. d). $\mathcal{T}_0^{\varepsilon,h} = (0.04, 1/32)$, e). $\frac{1}{4}\mathcal{T}_0^{\varepsilon,h}$, f). $\frac{1}{16}\mathcal{T}_0^{\varepsilon,h}$. Here $h = O(\varepsilon), k$ is independent of ε.

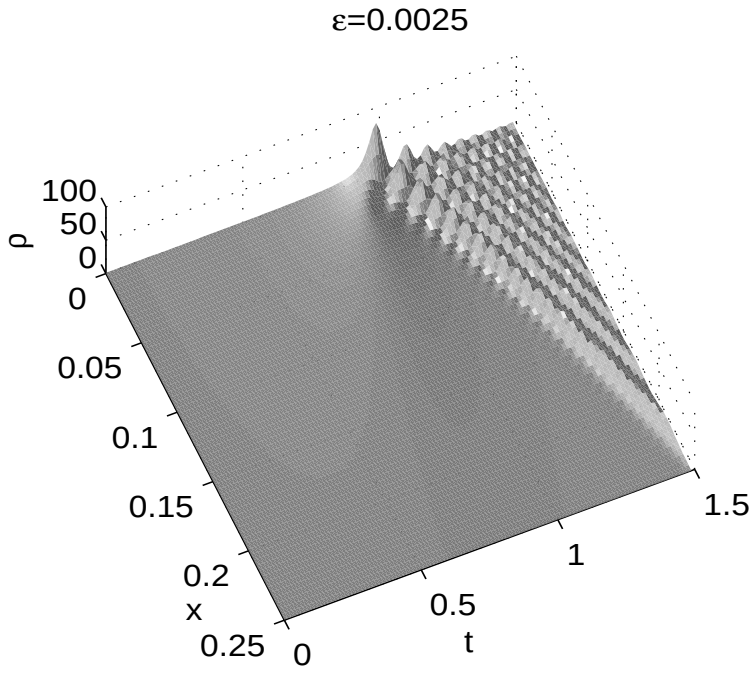

Figure 8: Evolution of the position density in Example 4 for $\varepsilon = 0.0025$.

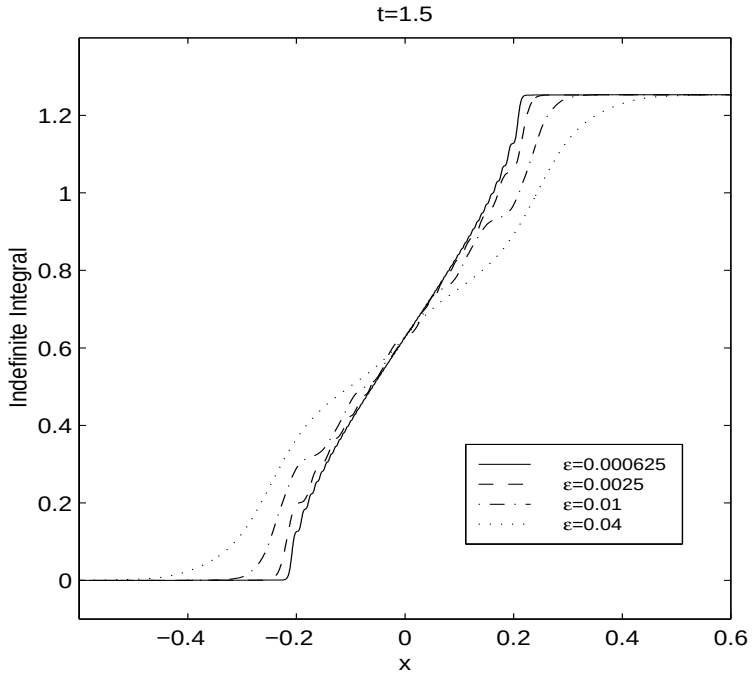

Figure 9: Indefinite integrals of the density $\rho^\varepsilon(x, t = 1.5)$ in Example 4 illustrating weak convergence.

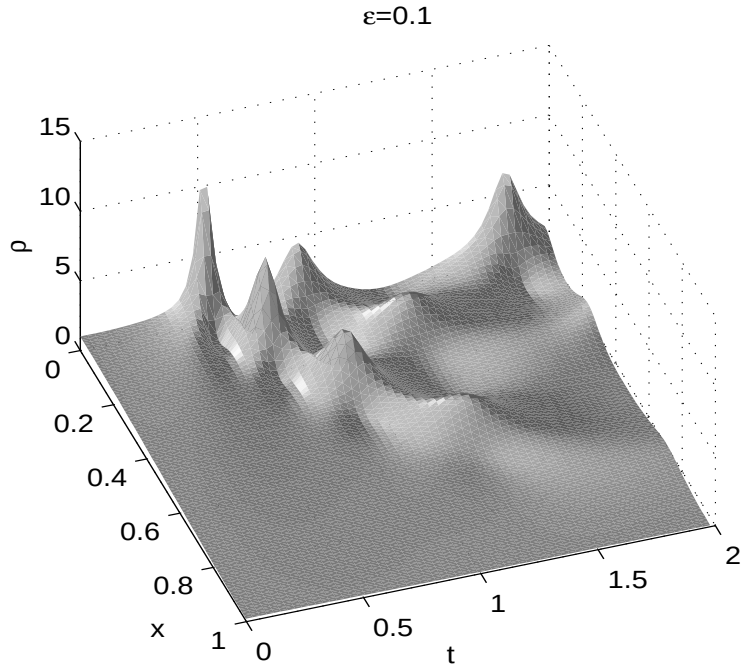

Figure 10: Evolution of the position density in Example 5 with zero initial phase data for $\varepsilon = 0.1$.

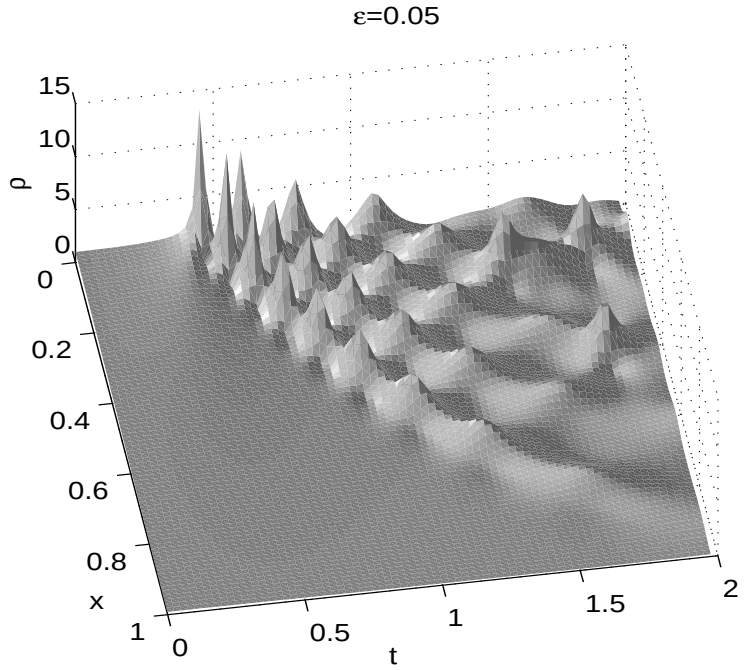

Figure 11: Evolution of the position density in Example 5 with zero initial phase data for $\varepsilon = 0.05$.

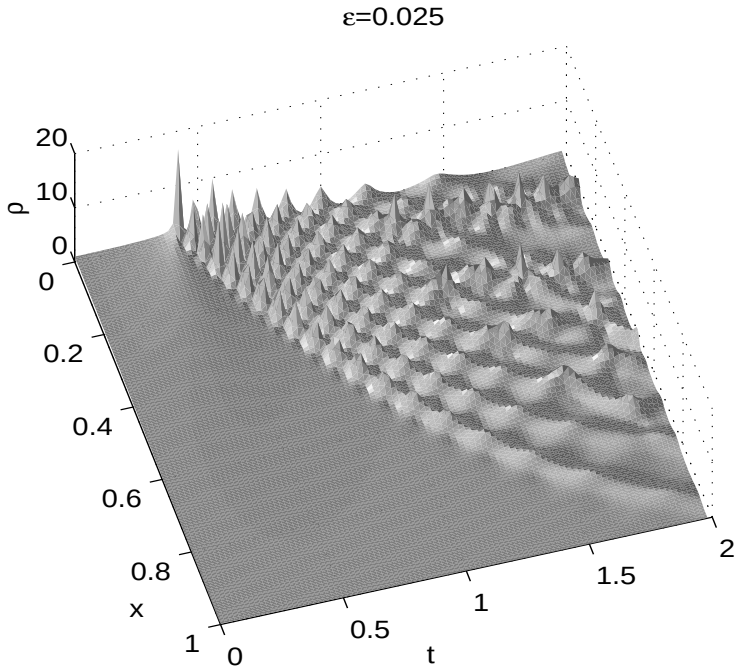

Figure 12: Evolution of the position density in Example 5 with zero initial phase data for $\varepsilon = 0.025$.

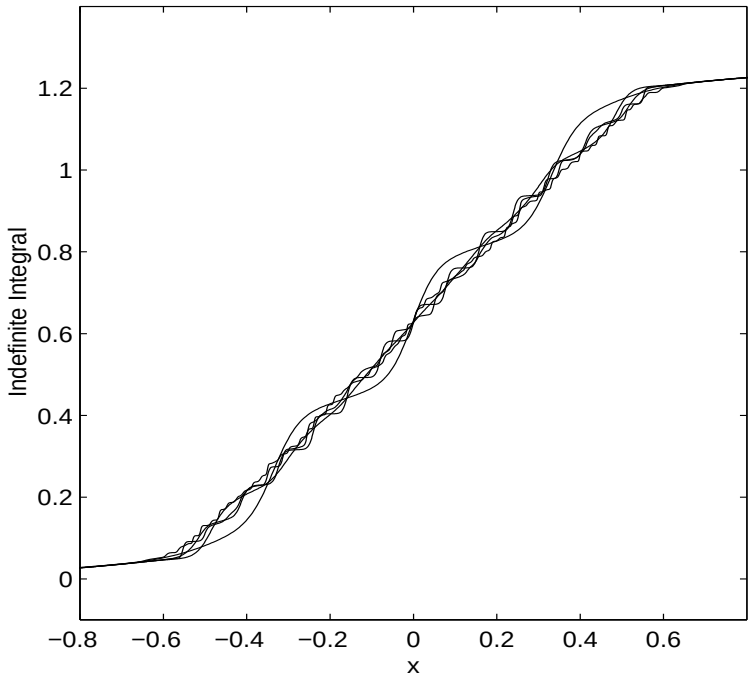

Figure 13: Indefinite integrals of the density $\rho^\varepsilon(x, t = 1.2)$ in Example 5 with zero initial phase data illustrating weak convergence. Curves with more "corners" correspond to smaller ε's, with $\varepsilon = 0.1$, 0.05, 0.025, 0.0125 and 0.00625.

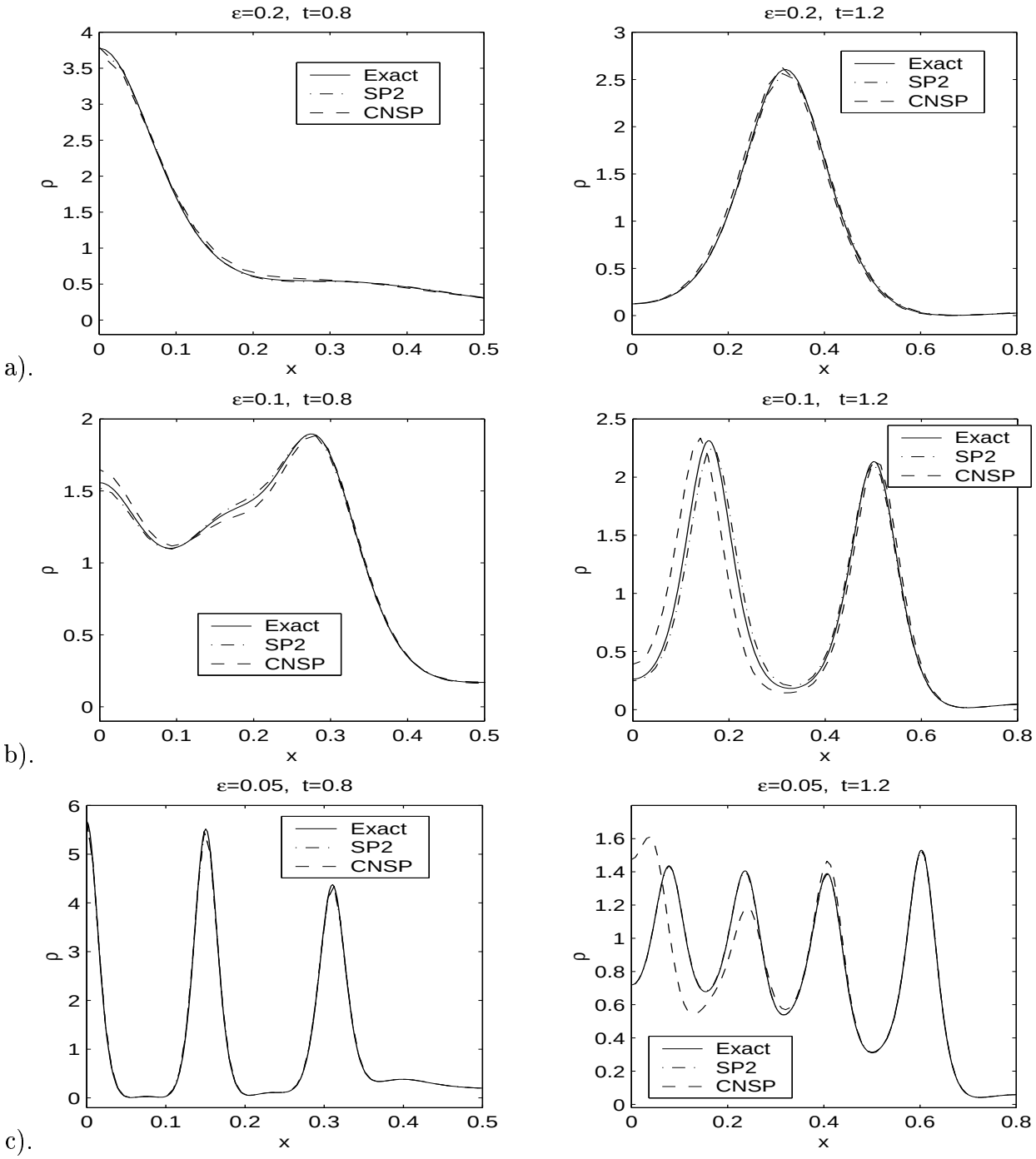

Figure 14: Comparison of SP2 and CNSP in Example 5 for zero initial phase data. '—': 'exact' solution', '+ + +': solution by SP2, 'x x x': solution by CNSP. a). $\mathcal{T}_0^{\varepsilon,h} = (0.2, 1/32)$ and $k_0 = 0.01$; b). $\frac{1}{2}\mathcal{T}_0^{\varepsilon,h}$ and $\frac{1}{4}k_0$; c). $\frac{1}{4}\mathcal{T}_0^{\varepsilon,h}$ and $\frac{1}{40}k_0$. Here $h = O(\varepsilon), k = o(\varepsilon)$.

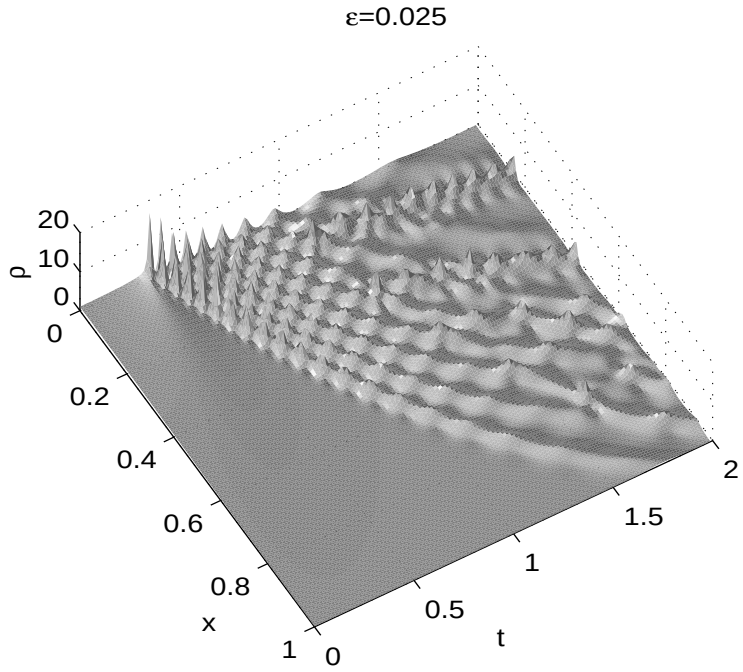

Figure 15: Evolution of the position density in Example 5 with nonzero initial phase data for $\varepsilon = 0.025$.

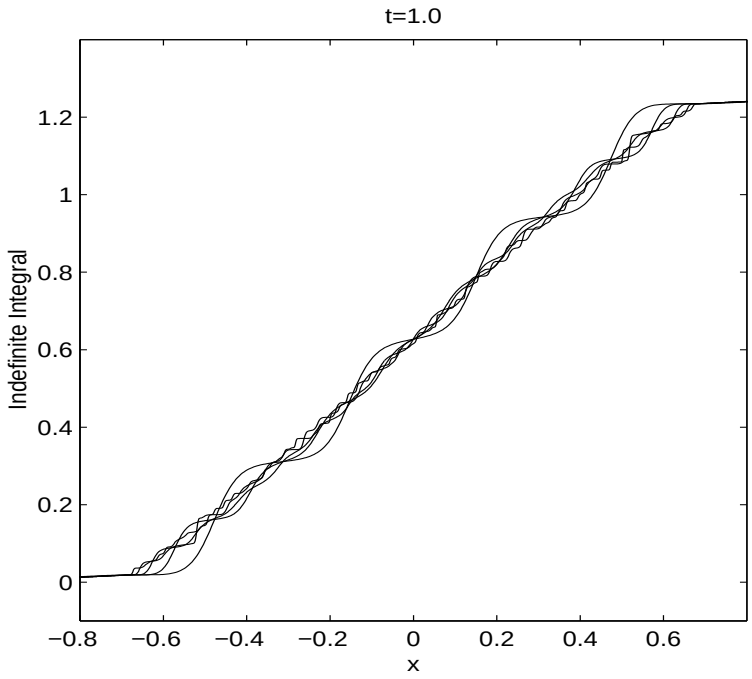

Figure 16: Indefinite integrals of the density $\rho^\varepsilon(x, t = 1.0)$ in Example 5 with nonzero initial phase data illustrating weak convergence. Curves with more "oscillations" correspond to smaller ε. Here $\varepsilon = 0.1$, 0.05, 0.025, 0.0125 and 0.00625.

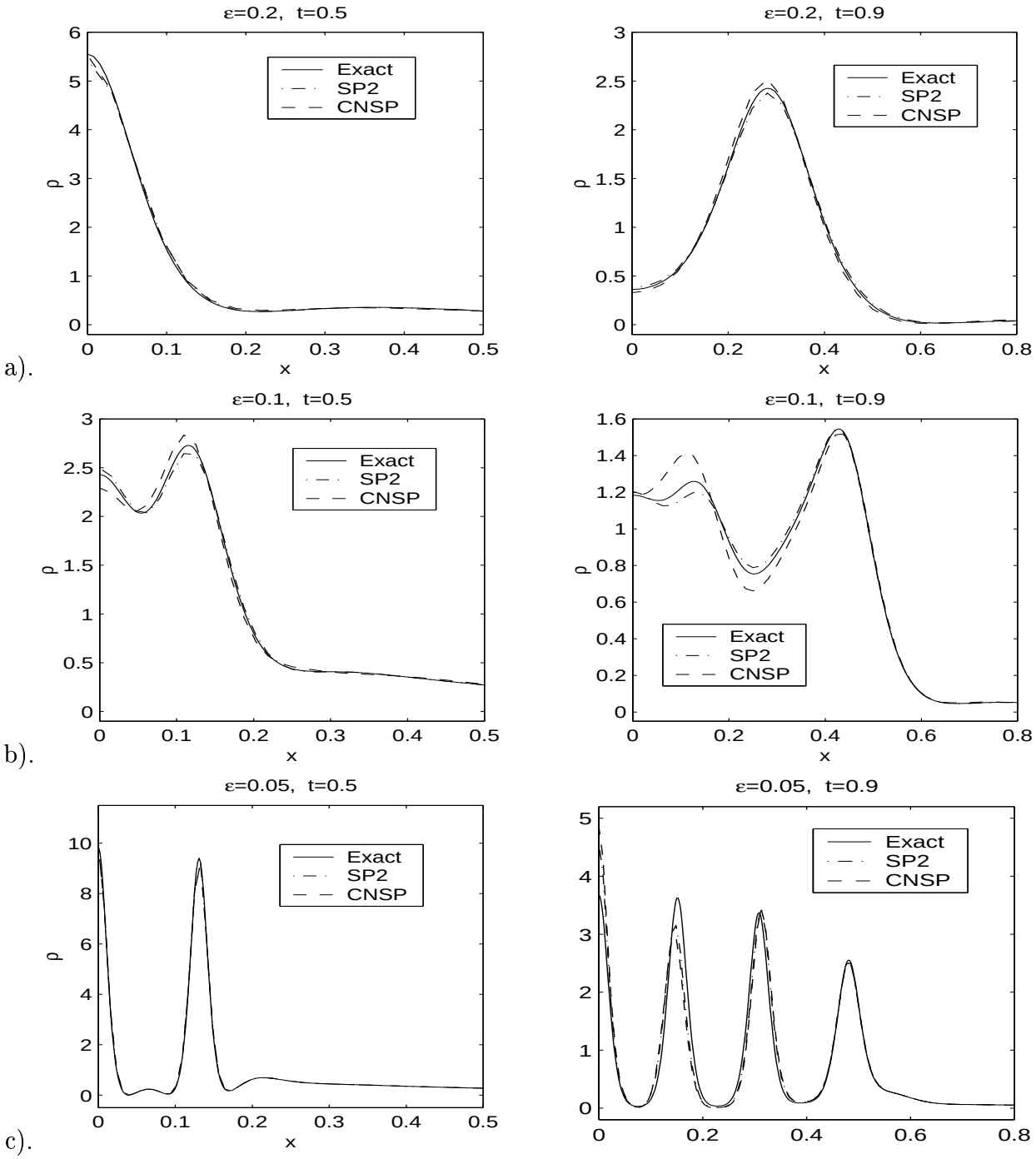

Figure 17: Comparison of SP2 and CNSP in Example 5 for nonzero initial phase data. '—': 'exact' solution', '+ + +': solution by SP2, 'x x x': solution by CNSP. a). $\mathcal{T}_0^{\varepsilon,h} = (0.2, 1/32)$ and $k_0 = 0.01$; b). $\frac{1}{2}\mathcal{T}_0^{\varepsilon,h}$ and $\frac{1}{4}k_0$; c). $\frac{1}{4}\mathcal{T}_0^{\varepsilon,h}$ and $\frac{1}{40}k_0$. Here $h = O(\varepsilon), k = o(\varepsilon)$.

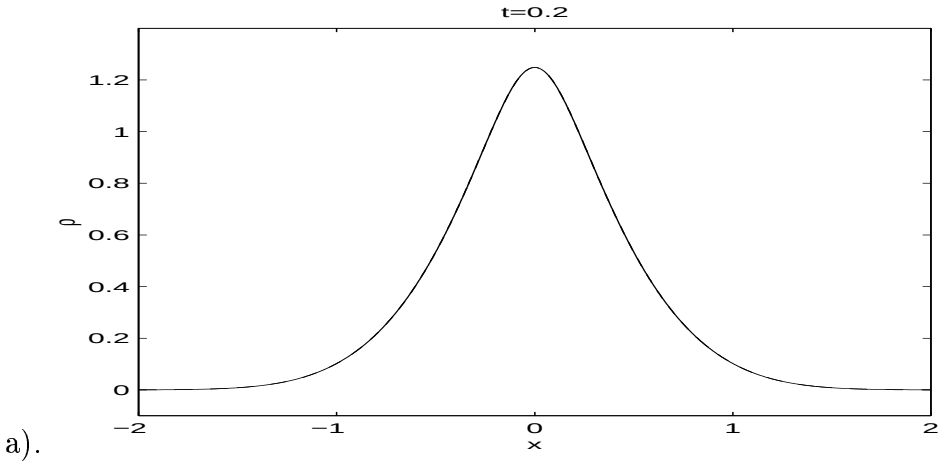

a).

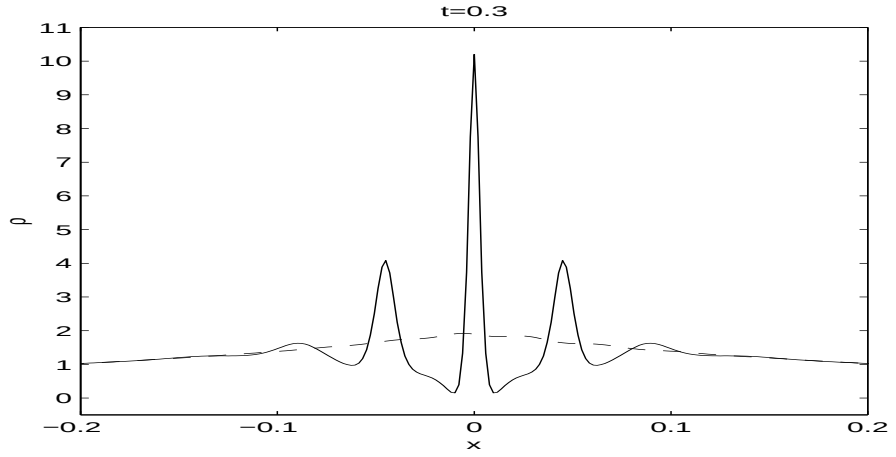

b).

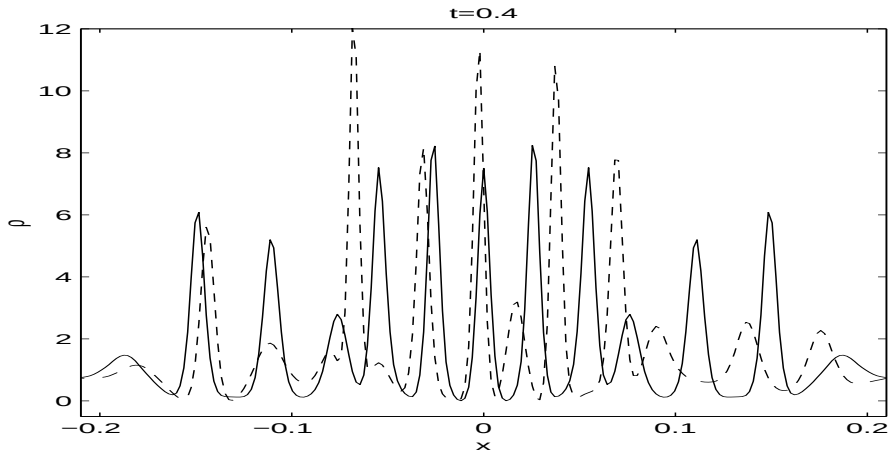

c).

Figure 18: Comparison of SP2 with and without Krasny's filter in Example 5 for nonzero initial phase data. '—': solution by SP2 with filter (keeping symmetry), '- - -': solution by SP2 without filter (losing symmetry). a). $t = 0.2$; b). $t = 0.3$; c). $t = 0.4$.

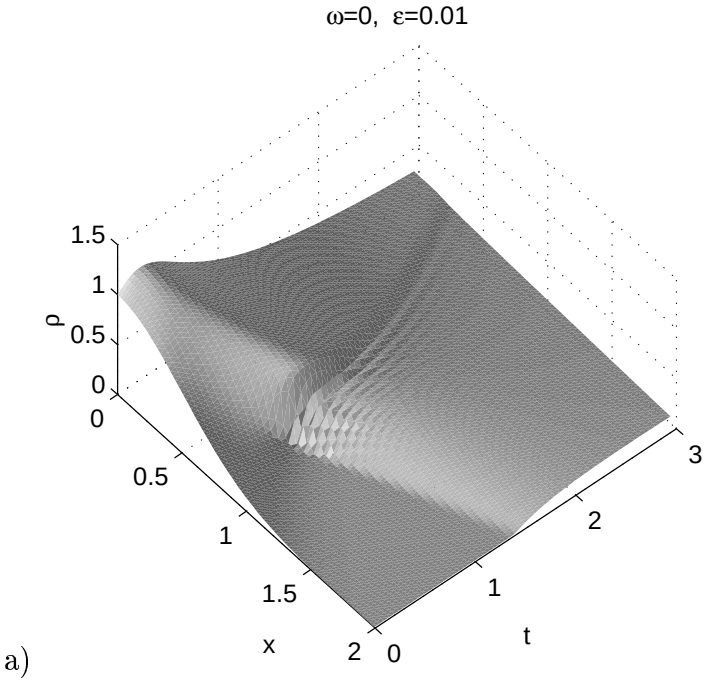

a)

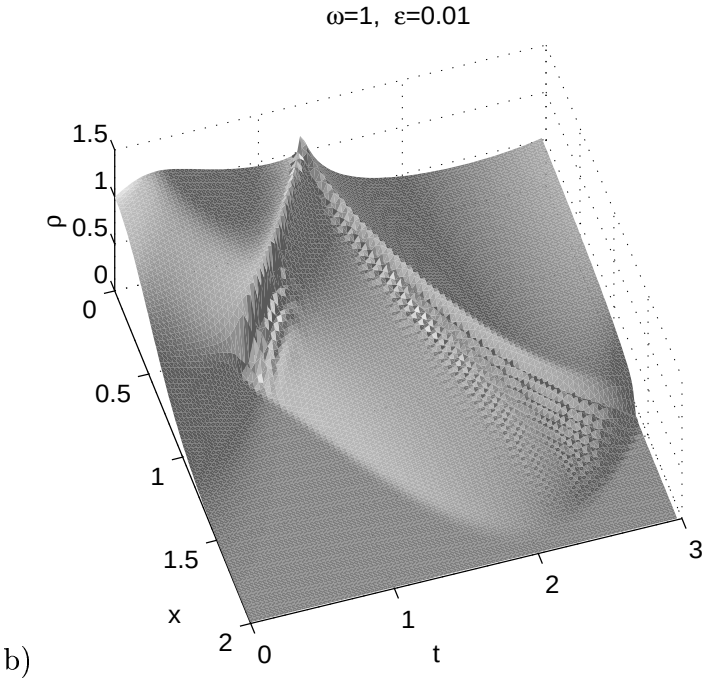

b)

Figure 19: Evolution of the position density in Example 6 for the defocusing case, i.e. $\beta = 1$, $\varepsilon = 0.01$. a). $\omega = 0$, b). $\omega = 1.0$.

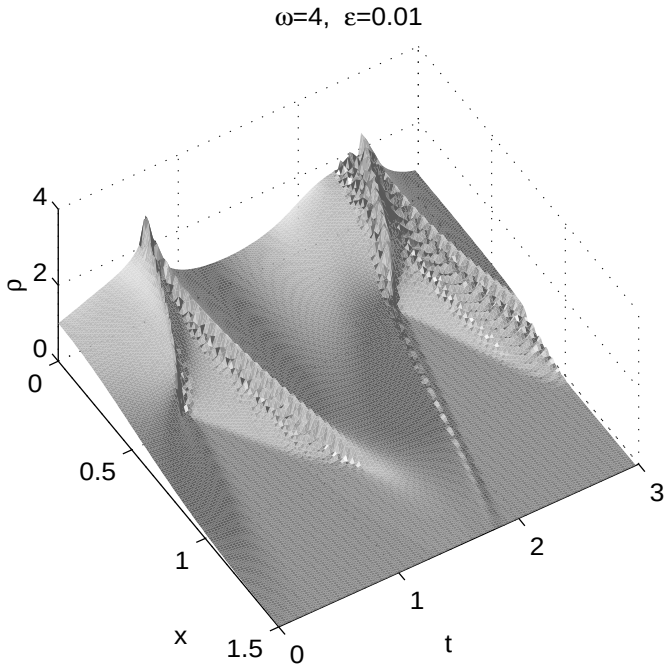

c)

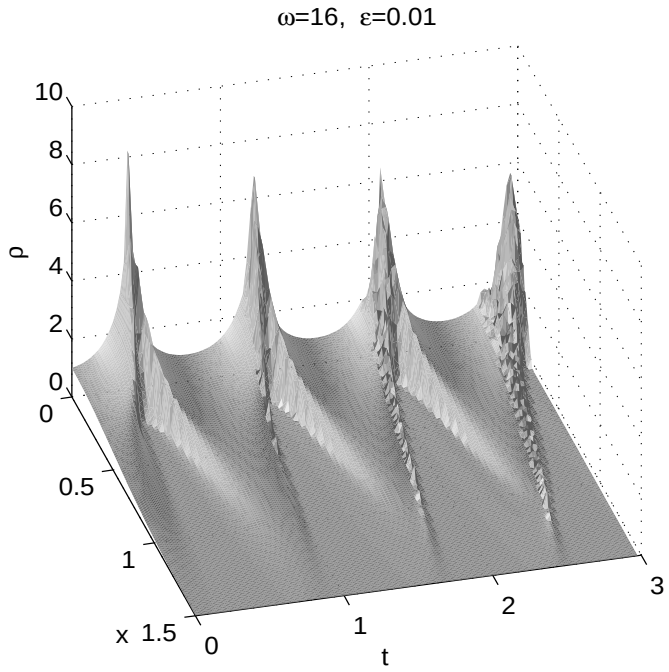

d)

Figure 19 (cont'd). c). $\omega = 4.0$, d). $\omega = 16.0$.

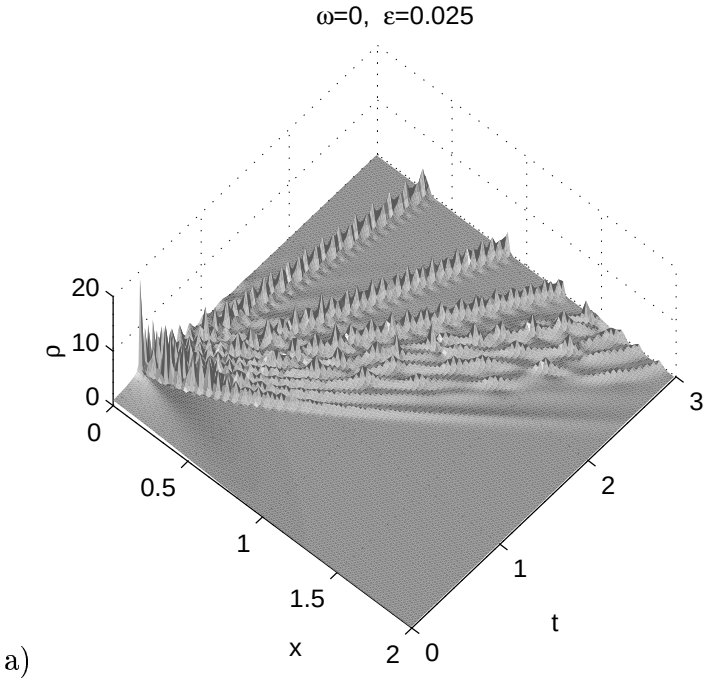

a)

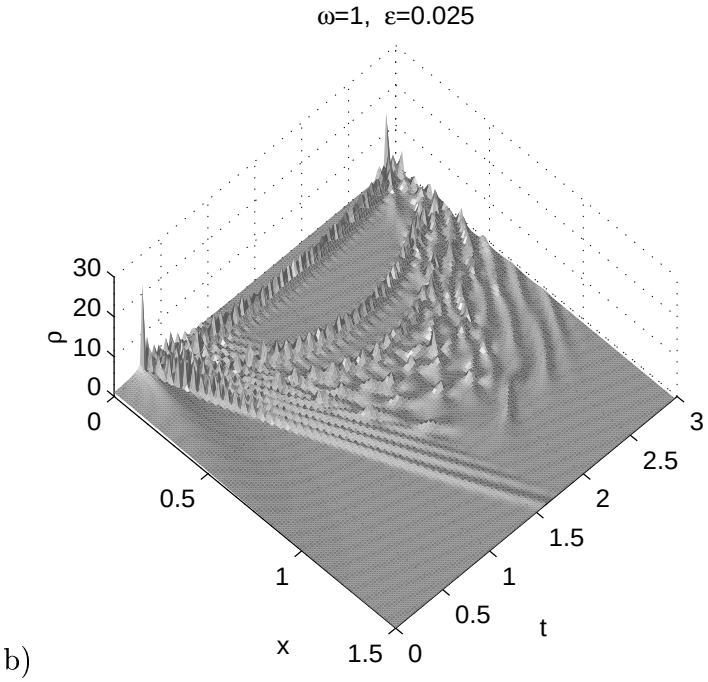

b)

Figure 20: Evolution of the position density in Example 6 for the focusing case, i.e. $\beta = -1$, $\varepsilon = 0.025$. a). $\omega = 0$, b). $\omega = 1.0$.

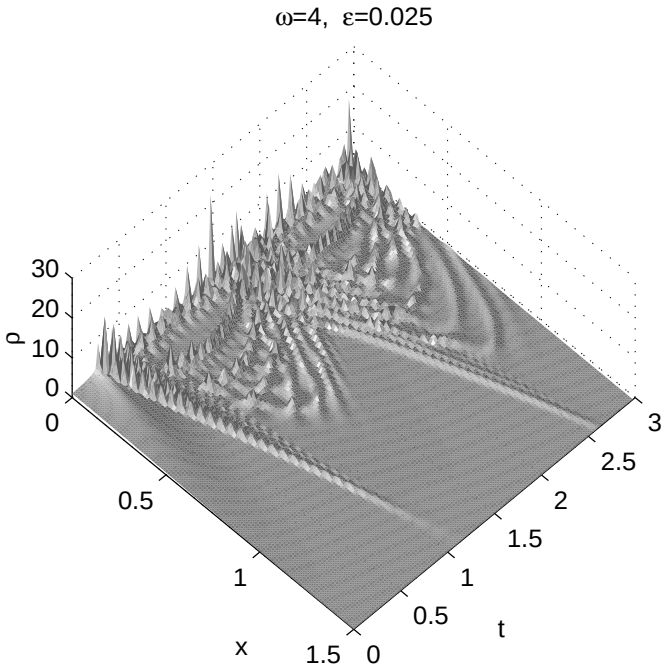

c)

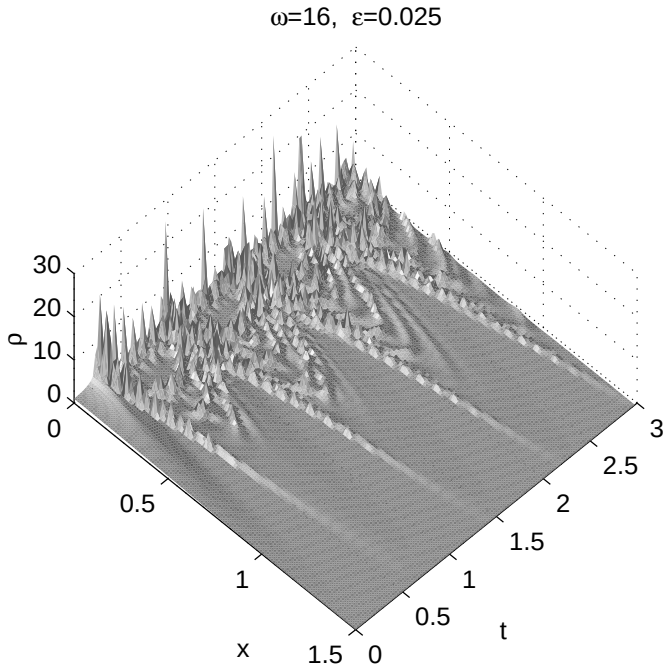

d)

Figure 20 (cont'd). c). $\omega = 4.0$, d). $\omega = 16.0$.

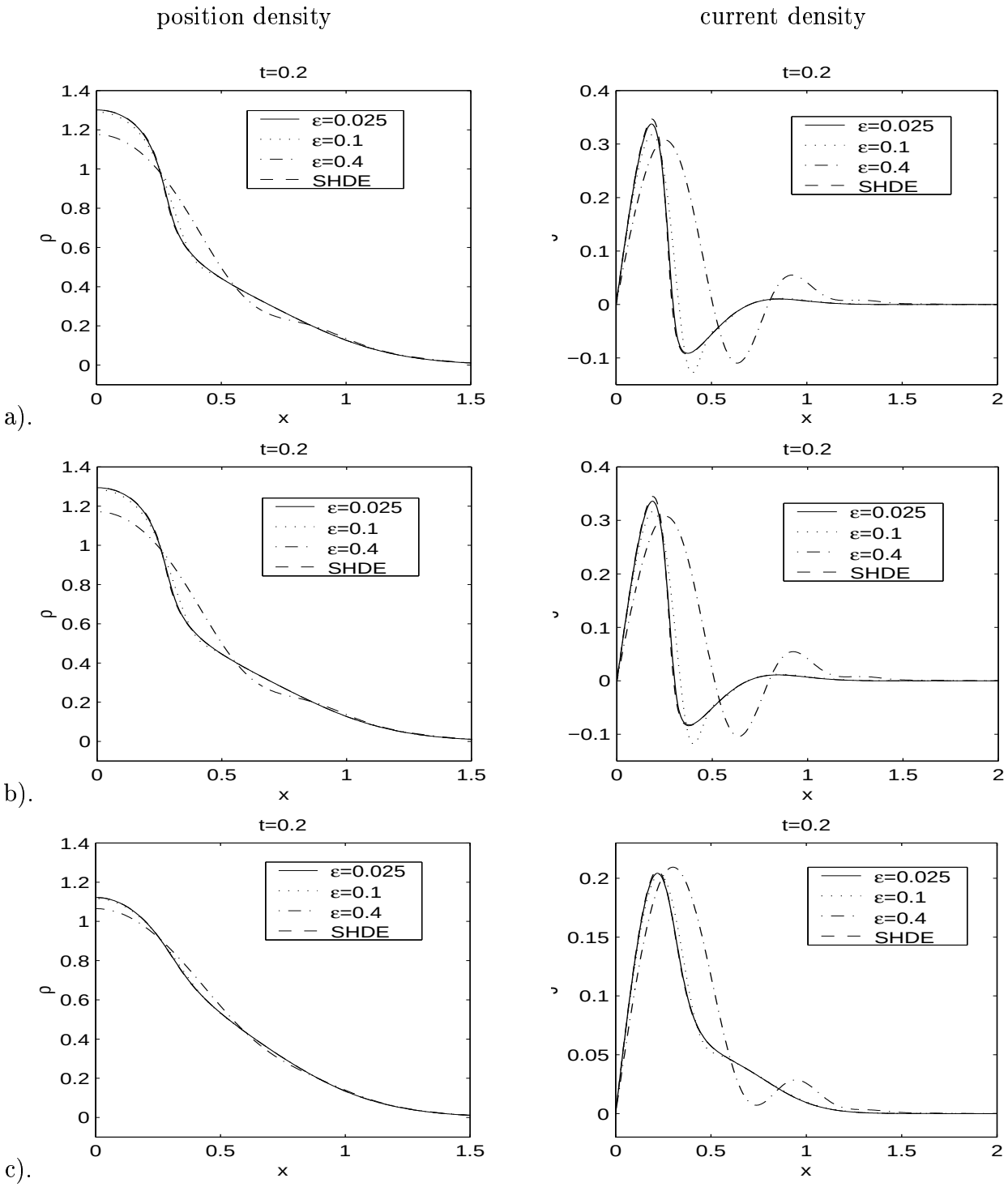

Figure 21: Numerical solutions in Example 7. a). $\tau = 0.0$, b). $\tau = 0.2$, c). $\tau = 10.0$. I. $\gamma = 2.0$, at time $t = 0.2$.

position density

current density

d).

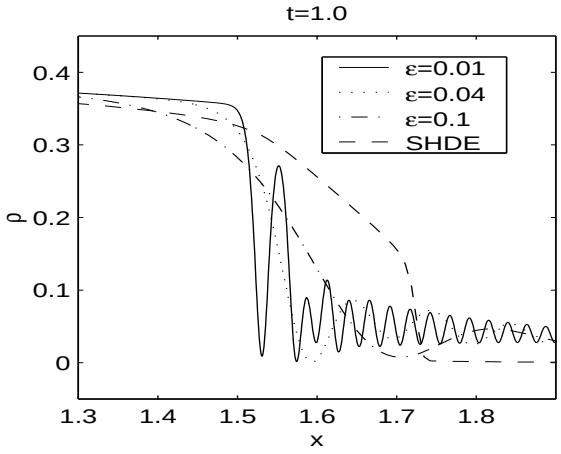

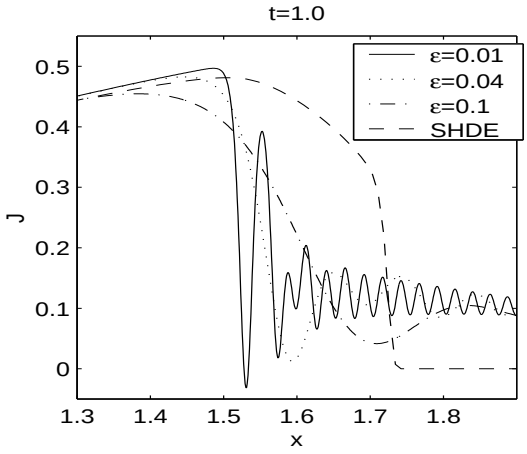

e).

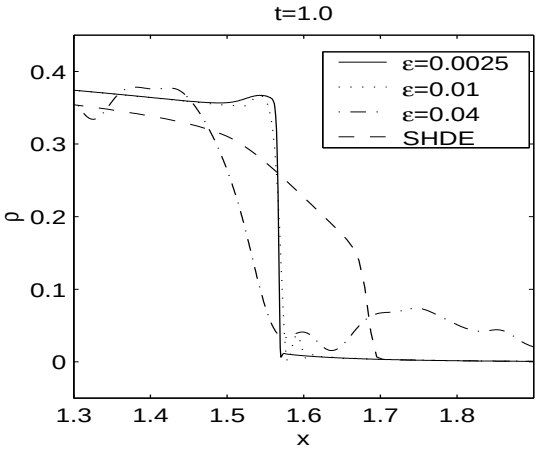

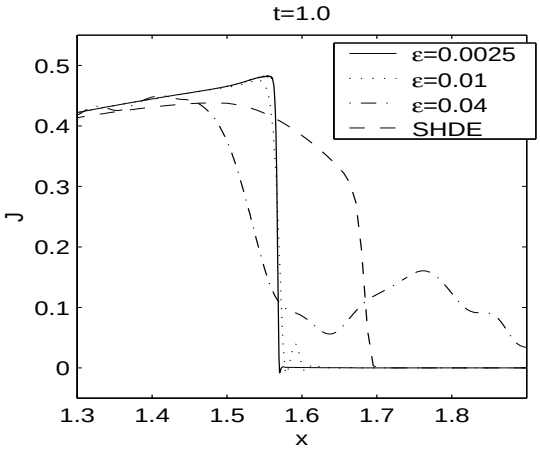

f).

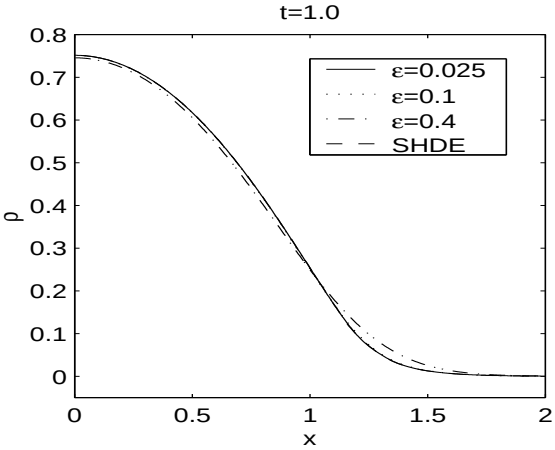

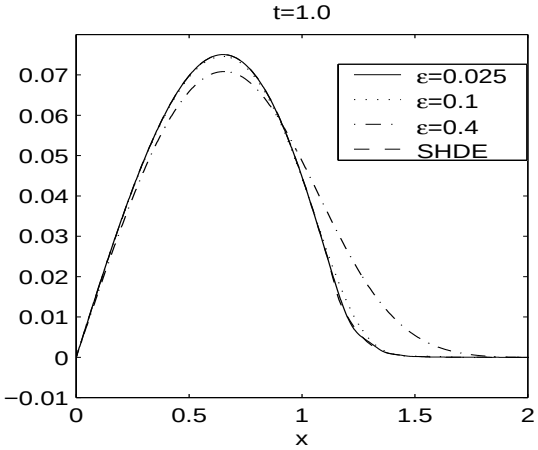

Figure 21 (cont'd): II. $\gamma = 2.0$, at time $t = 1.0$. d). $\tau = 0.0$, e). $\tau = 0.2$, f). $\tau = 10.0$.

position density

current density

g).

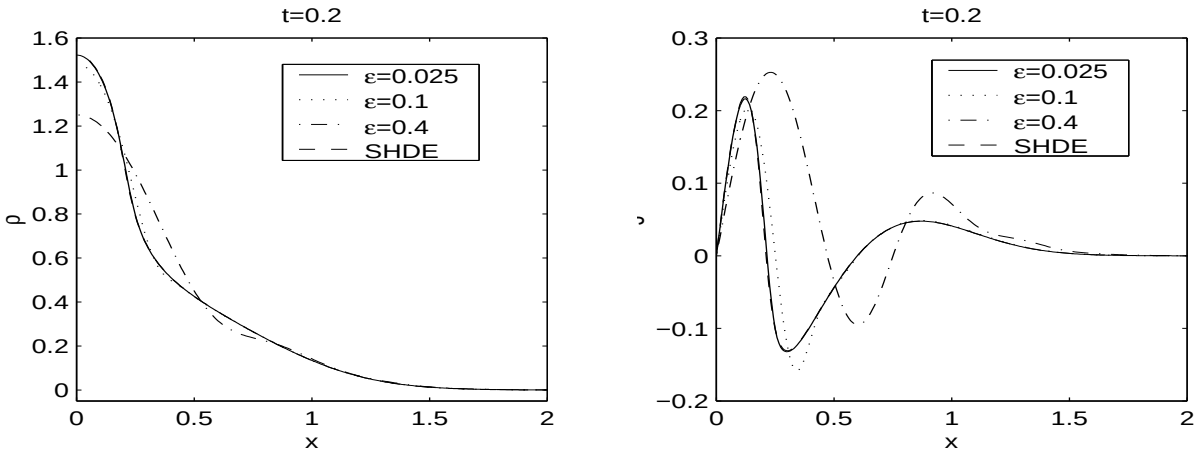

h).

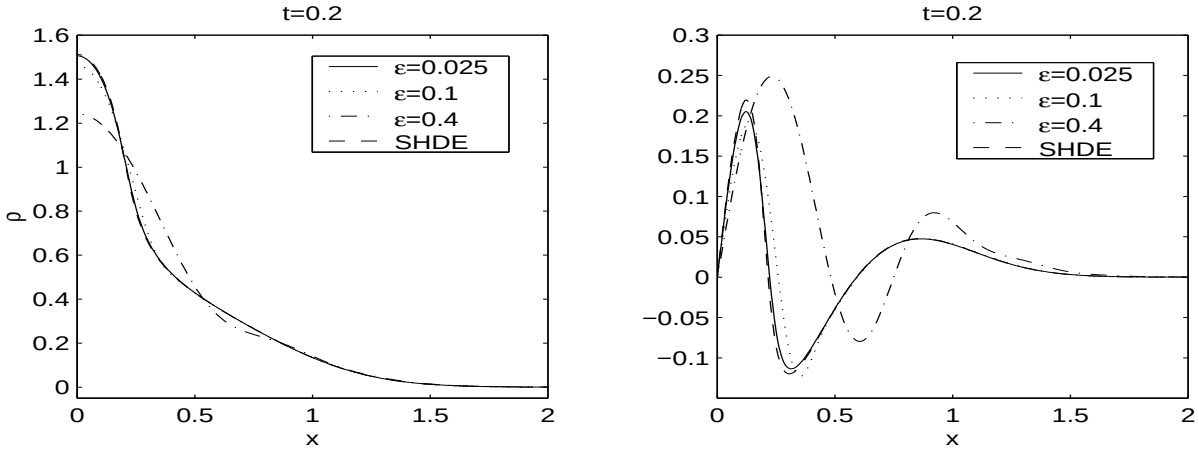

i).

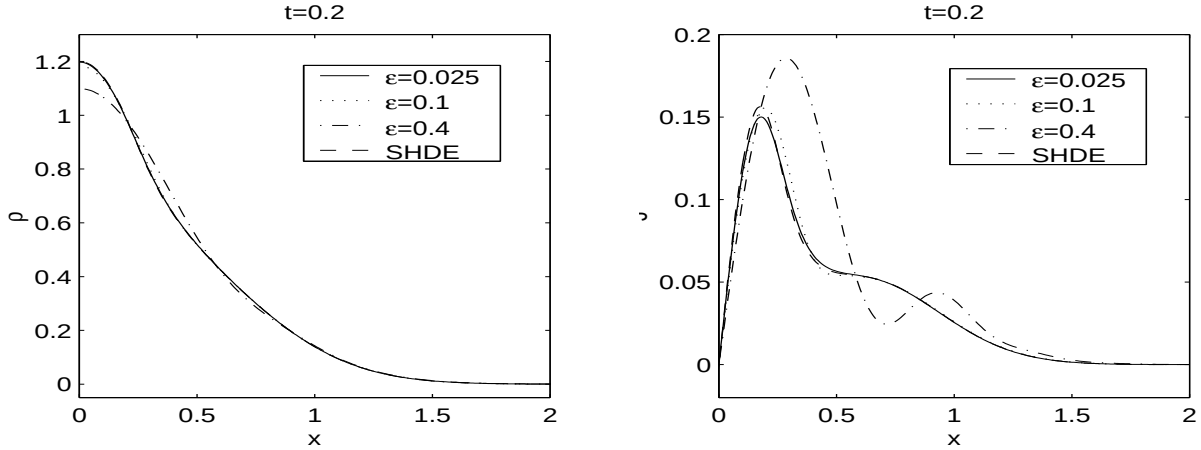

Figure 21 (cont'd): III. $\gamma = 1.4$, at time $t = 0.2$. g). $\tau = 0.0$, h). $\tau = 0.2$, i). $\tau = 10.0$.

position density

current density

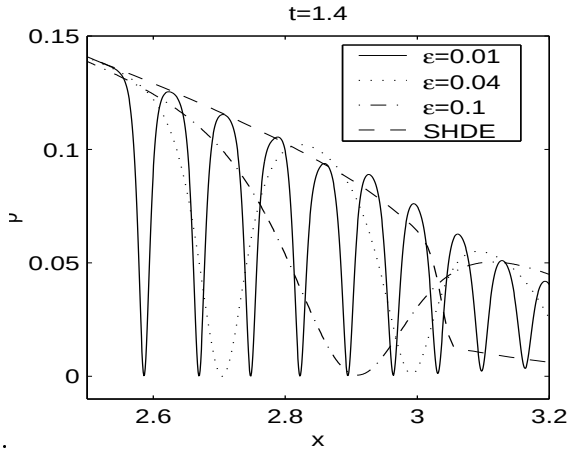

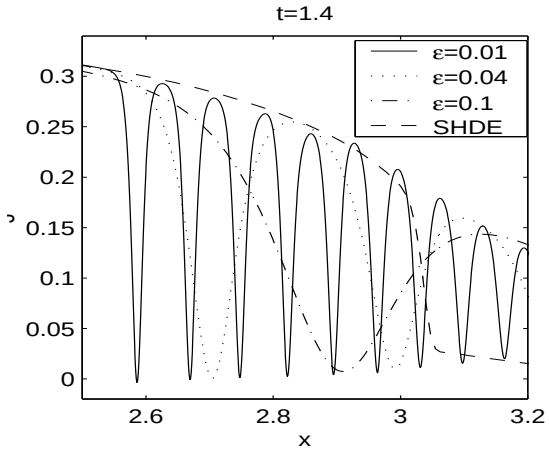

j).

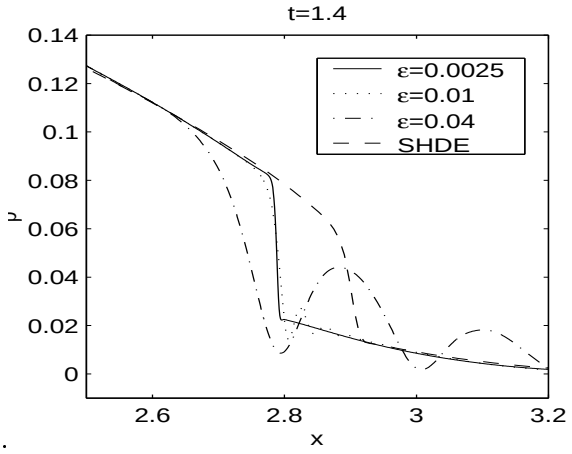

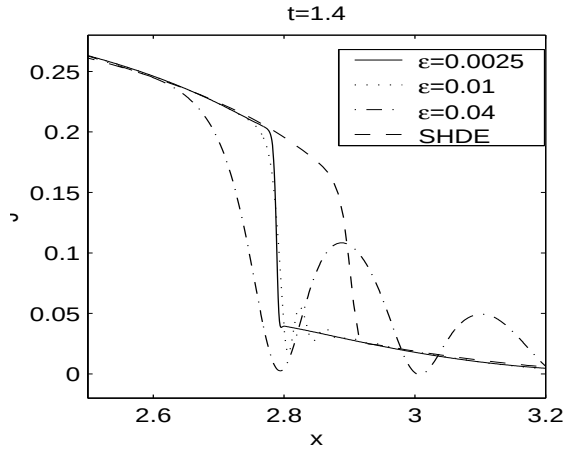

k).

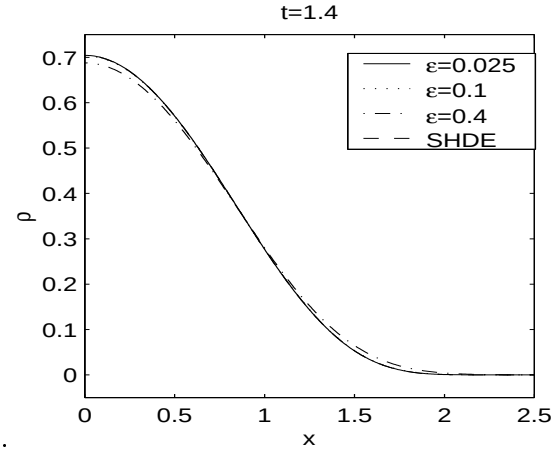

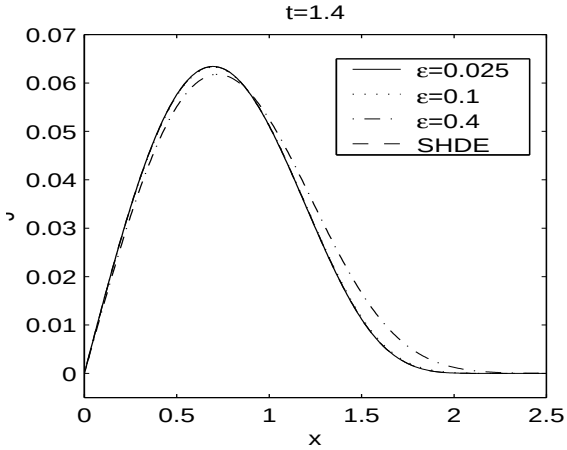

l).

Figure 21 (cont'd): IV. $\gamma = 1.4$, at time $t = 1.4$. j). $\tau = 0.0$, k). $\tau = 0.2$, l). $\tau = 10.0$.

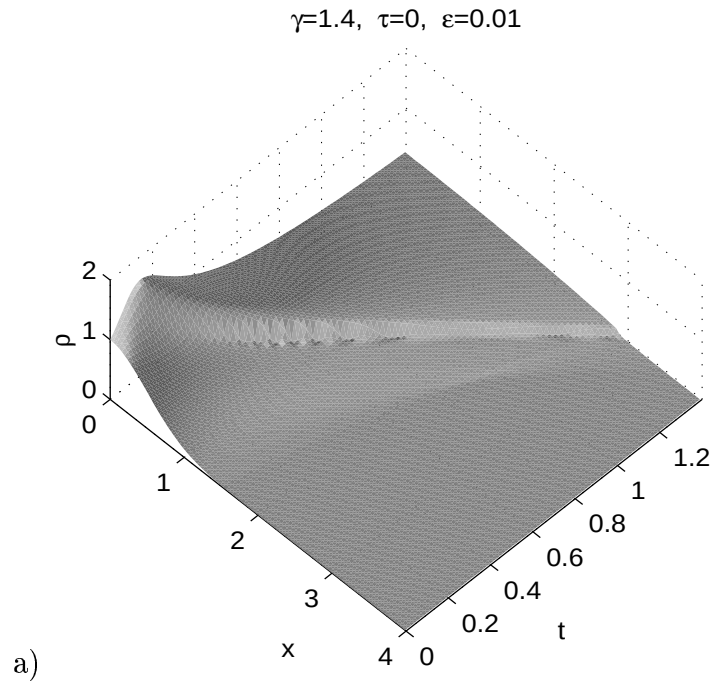

a)

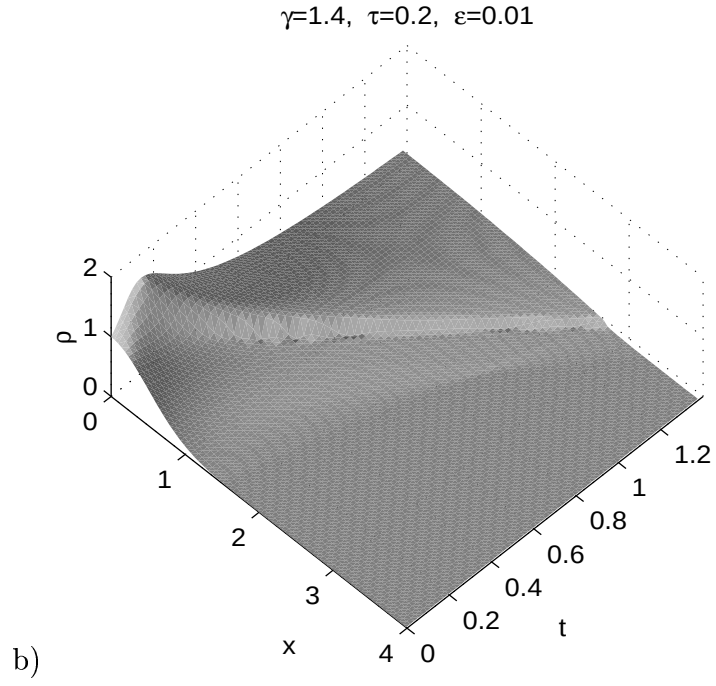

b)

Figure 22: Evolution of the position density in Example 7 for the defocusing case, i.e. $\gamma = 1.4$, $\varepsilon = 0.01$. a). $\tau = 0.0$, b). $\tau = 0.2$.

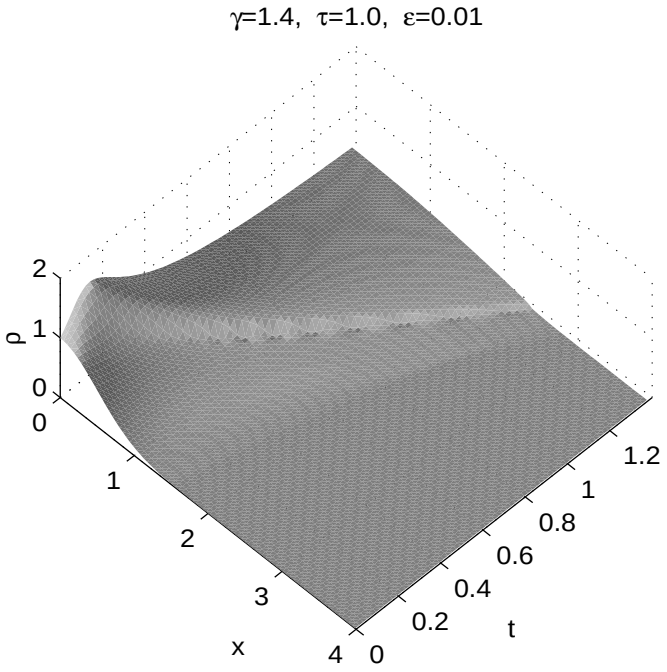

c)

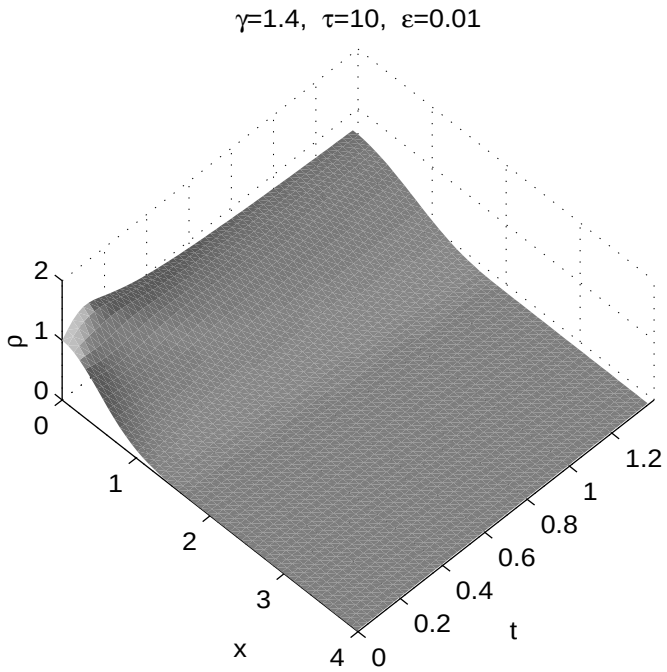

d)

Figure 22 (cont'd). c). $\tau = 1.0$, d). $\tau = 10.0$.